

**2-DIMENSIONAL INFRARED SPECTROSCOPY AND ITS APPLICATION TO THE  
STUDY OF PROTEIN METAL-BINDING LIGANDS**

by

**Duane A. Couchot-Vore**

B.S., Chemistry, Shawnee State University, 2007

Submitted to the Graduate Faculty of  
The Kenneth P. Dietrich School of Arts and Sciences in partial fulfillment  
of the requirements for the degree of  
Master of Science

University of Pittsburgh

2014

**UNIVERSITY OF PITTSBURGH**

**The Kenneth P. *Dietrich* School of Arts and Sciences**

This thesis was presented

by

Duane A. Couchot-Vore

It was defended on

02/06/2014

and approved by

Dr. Sunil Saxena, Professor, Department of Chemistry

Dr. Daniel Lambrecht, Assistant Professor, Department of Chemistry

Thesis Director: Dr. Sean Garrett-Roe, Assistant Professor, Department of Chemistry

**2-DIMENSIONAL INFRARED SPECTROSCOPY AND ITS APPLICATION TO THE  
STUDY OF PROTEIN METAL-BINDING LIGANDS**

Duane Couchot-Vore, M.S.

University of Pittsburgh, 2014

Copyright © by Duane Couchot-Vore

2014

**2-DIMENSIONAL INFRARED SPECTROSCOPY AND ITS APPLICATION TO THE  
STUDY OF PROTEIN METAL-BINDING LIGANDS**

**Duane A. Couchot-Vore, M.S.**

**University of Pittsburgh, 2014**

The binding of protein to metal ions is essential to the functioning of thousands of enzymes. Although the action of many proteins is well known, there is less concrete knowledge about the mechanisms behind them because traditional methods such as NMR are orders of magnitude too slow to observe the dynamics. Two-dimensional infrared spectroscopy is able to probe molecular structure and dynamics on the sub-picosecond time scale. The fundamentals of 2D-IR spectroscopy is developed to enable the understanding of the process. The binding sites of many proteins such as those containing the widespread EF-hand motif rely on carbonyl ligands, both backbone amides and side-chain carboxylates. Butyramide and EDTA are analyzed with linear Fourier-transform and two-dimensional infrared spectroscopy. The data are consistent with published literature. Butyramide shows a binding time scale with water of 600 fs, which is consistent with the known weak binding of amides to metal in aqueous solutions. Vibrational

frequencies are calculated using density functional theory. The carboxylate normal modes of calcium-bound EDTA show delocalization and energy splitting consistent with vibrational excitons.

## TABLE OF CONTENTS

<b>ABSTRACT</b> .....	<b>IV</b>
<b>PREFACE</b> .....	<b>XVIII</b>
<b>1.0 INTRODUCTION</b> .....	<b>1</b>
<b>2.0 THEORY</b> .....	<b>6</b>
<b>2.1.1 Describing Molecular Vibrations</b> .....	<b>6</b>
<b>2.1.1.1 Basic Oscillator Models</b> .....	<b>6</b>
<b>2.1.1.2 The Density Matrix and Ensembles</b> .....	<b>10</b>
<b>2.1.1.3 Vibrational Excitons</b> .....	<b>14</b>
<b>2.1.2 Interaction with Radiation</b> .....	<b>15</b>
<b>2.1.2.1 The Response Function</b> .....	<b>15</b>
<b>2.1.2.2 Polarization</b> .....	<b>16</b>
<b>2.1.3 Feynman Diagrams and Rephasing</b> .....	<b>19</b>
<b>2.1.4 Implementation</b> .....	<b>22</b>
<b>2.1.4.1 Overview</b> .....	<b>22</b>
<b>2.1.4.2 Generating the <math>\omega_1</math> axis</b> .....	<b>23</b>
<b>2.1.4.3 Phase matching</b> .....	<b>24</b>
<b>2.1.4.4 The Local Oscillator</b> .....	<b>25</b>
<b>2.1.5 Spectroscopic Observables</b> .....	<b>25</b>

2.1.5.1	Classical Spectroscopic Processes and Anharmonicity .....	25
2.1.5.2	Spectral Diffusion.....	27
2.1.5.3	Cross Peaks .....	29
3.0	MATERIALS AND METHODS .....	31
4.0	RESULTS AND DISCUSSION .....	33
4.1	AMIDE.....	33
4.1.1	General .....	33
4.1.2	Blue shift of butyramide amide I peak with salt concentration .....	34
4.1.3	Correlation Function.....	35
4.1.4	Red shift of butryamide-D <sub>2</sub> O amide I with salt concentration.....	37
4.1.5	Comparison with simulation results .....	39
4.2	CARBOXYLATE .....	40
4.2.1	General .....	40
4.2.2	Blue shift of EDTA carboxylate asymmetric stretch peak with salt concentration .....	42
4.2.3	Simulation Results .....	42
4.2.3.1	General Considerations .....	42
4.2.3.2	Comparison of Experimental and Computational Results .....	43
4.2.4	Initial investigation into EDTA vibrational excitons.....	46
5.0	CONCLUSION.....	49
	APPENDIX A .....	50
	APPENDIX B .....	52
	APPENDIX C .....	53

<b>APPENDIX D</b> .....	<b>55</b>
<b>APPENDIX E</b> .....	<b>58</b>
<b>BIBLIOGRAPHY</b> .....	<b>61</b>



## LIST OF TABLES

Table 1: Results of Q-Chem simulation of butyramide systems .....	40
Table 2: Measured vs simulated results for EDTA binding .....	44
Table 3: Calculated spectroscopic bands corresponding to carboxylate asymmetric stretch. ....	45
Table 4: Computed coupling values for EDTA systems. ....	48

## LIST OF FIGURES

Figure 1. Detail of the EF-hand binding loop showing detail side-chain carboxylate and backbone and side-chain amide ligands.....	1
Figure 2. Representation of charge transfer vs. polarization .....	3
Figure 3: Comparison of the Morse potential with a harmonic oscillator. ....	7
Figure 4: The widening of a potential well by external forces compresses the energy levels.....	8
Figure 5: The first three probability waves of the quantum harmonic oscillator.....	10
Figure 6: Illustration of a pure state and a mixed state with the same net vector. ....	12
Figure 7 Dephasing because of variations in energy environment .....	13
Figure 8: Timing sequence of a third-order spectroscopy .....	17
Figure 9: Feynman diagrams for $R_1$ and $R_1^*$ pathways .....	19
Figure 10: Rephasing vs non-rephasing pathways.....	21
Figure 11: How timing changes can determine a frequency.....	23
Figure 12: Propagation vectors .....	24
Figure 13: Phase matching with Feynman Diagrams .....	25
Figure 14: The three classical spectroscopic processes .....	26
Figure 15. Essentials of a 2D IR spectrum, showing anharmonicity.....	26
Figure 16: Spectral diffusion .....	27

Figure 17: Methods of measuring spectral diffusion .....	28
Figure 18: Weak and strong coupling domains .....	29
Figure 19: Butyramide-Ca <sup>2+</sup> sequence take against an N <sub>2</sub> background.....	33
Figure 20: 200 mM butyramide in D <sub>2</sub> O with various concentrations of Ca <sup>2+</sup> and Mg <sup>2+</sup> .....	34
Figure 21: Fitted 2D-IR spectra of butyramide in D <sub>2</sub> O at 200, 600, 1200 fs population time.....	36
Figure 22: Single-exponential correlation fit of butyramide/D <sub>2</sub> O spectral diffusion based on centerline slope. ....	36
Figure 23: Proposed spectral shift scenario in weak metal ion binding to butyramide .....	37
Figure 24: Visualization of the butyramide-Ca model .....	39
Figure 25: FTIR spectra of EDTA/Mg <sup>2+</sup> at various concentrations of Mg <sup>2+</sup> .....	40
Figure 26: FTIR spectra of 250mM EDTA-D <sub>4</sub> in D <sub>2</sub> O with various concentrations of Ca <sup>2+</sup> and Mg <sup>2+</sup> with D <sub>2</sub> O background .....	41
Figure 27: Protonation states of EDTA .....	42
Figure 28: Local mode motions derived from a butyrate model .....	42
Figure 29: Determination of local-mode dipole in EDTA complex .....	43
Figure 30: Vibrational modes of EDTA corresponding to the carboxylate-Ca asymmetric stretch frequencies as calculated by Q-Chem.....	45
Figure 31: Stick plot of EDTA carboxylate antisymmetric stretch frequencies.....	46
Figure 32: Rotational symmetry of EDTA vibrational modes.....	46
Figure 33: Schematic of EDTA .....	46
Figure 34: Right-handed exponential function .....	56

## LIST OF EQUATIONS

$\hat{H} \psi\rangle = E \psi\rangle$ 1 .....	7
$V(r) = D_e \left(1 - e^{-a(r-r_e)}\right)^2$ 2 .....	7
$\hat{H} = \frac{\hat{p}^2}{2m} + \frac{1}{2}m\omega^2\hat{x}^2 = -\hbar\frac{\partial^2}{dx^2} + \frac{1}{2}m\omega^2\hat{x}^2$ 3 .....	7
$E_\nu = \hbar\omega\left(\nu + \frac{1}{2}\right)$ . 4 .....	7
$\omega = \sqrt{\frac{k}{\mu}}$ . 5 .....	8
$\hat{H} = \hat{H}_0 + \hat{H}'$ 6 .....	9
$E = \hbar\omega\left(\nu + \frac{1}{2}\right) - \hbar\omega\chi\left(\nu + \frac{1}{2}\right)^2$ , 7 .....	9
$i\hbar\frac{\partial}{\partial t} \psi\rangle = E \psi\rangle$ , 8 .....	9
$ \psi\rangle = \sum_n c_n e^{-iE_n t/\hbar}  n\rangle$ . 9 .....	10
$\psi_{01} = c_0 e^{-iE_0 t/\hbar} + c_1 e^{-iE_1 t/\hbar} = \begin{pmatrix} c_0 e^{-iE_0 t/\hbar} \\ c_1 e^{-iE_1 t/\hbar} \end{pmatrix}$ 10 .....	11

$$\begin{aligned} \rho &= |\psi\rangle\langle\psi| = \begin{pmatrix} c_0 e^{-iE_0 t/\hbar} |0\rangle \\ c_1 e^{-iE_1 t/\hbar} |0\rangle \end{pmatrix} \begin{pmatrix} c_0^* e^{iE_0 t/\hbar} \langle 1| & c_1^* e^{iE_1 t/\hbar} \langle 1| \end{pmatrix} \\ &= \begin{pmatrix} c_0^2 & c_0 c_1^* e^{i(E_1 - E_2)t/\hbar} \\ c_1 c_0^* e^{i(E_2 - E_1)t/\hbar} & c_1^2 \end{pmatrix} & 11 \dots\dots\dots 11 \\ &= \begin{pmatrix} c_0^2 & c_0 c_1^* e^{i\omega_0 t} \\ c_0^* c_1 e^{-i\omega_0 t} & c_1^2 \end{pmatrix} \end{aligned}$$

$$|0\rangle\langle 0| = \begin{pmatrix} 1 & 0 \\ 0 & 0 \end{pmatrix}, \quad |1\rangle\langle 1| = \begin{pmatrix} 0 & 0 \\ 0 & 1 \end{pmatrix}. \quad 12 \dots\dots\dots 11$$

$$\begin{pmatrix} \frac{1}{2} & -\frac{i}{2} e^{i\omega_0 t} \\ \frac{i}{2} e^{-i\omega_0 t} & \frac{1}{2} \end{pmatrix} \rightarrow \begin{pmatrix} 1 & 0 \\ 0 & 0 \end{pmatrix} \quad 13 \dots\dots\dots 12$$

$$\begin{pmatrix} \frac{1}{2} & -\frac{i}{2} e^{i\omega_0 t} \\ \frac{i}{2} e^{-i\omega_0 t} & \frac{1}{2} \end{pmatrix} \rightarrow \begin{pmatrix} \frac{1}{2} & 0 \\ 0 & \frac{1}{2} \end{pmatrix} \quad 14 \dots\dots\dots 12$$

$$\rho^{(1)} = \begin{pmatrix} c_0^2 & c_0 c_1^* e^{i\omega_0 t} e^{t/T_2} \\ c_0^* c_1 e^{-i\omega_0 t} e^{t/T_2} & c_1^2 \end{pmatrix} \quad 15 \dots\dots\dots 13$$

$$\frac{1}{T_2} = \frac{1}{2T_1} + \frac{1}{T_2^*}. \quad 16 \dots\dots\dots 13$$

$$\rho = \rho^{(0)} + \rho^{(1)} + \dots = \begin{pmatrix} 1 & 0 \\ 0 & 0 \end{pmatrix} + \begin{pmatrix} c_0^2 & -c_0 c_1^* e^{i\omega_0 t} \\ c_0^* c_1 e^{-i\omega_0 t} & c_1^2 \end{pmatrix} + \dots \quad 17 \dots\dots\dots 14$$

$$A = \langle\psi|\hat{A}|\psi\rangle \quad 18 \dots\dots\dots 14$$

$$E = \begin{pmatrix} |\psi_1\rangle \\ |\psi_2\rangle \\ |\psi_3\rangle \\ |\psi_4\rangle \end{pmatrix} \begin{pmatrix} \hat{H}_1 & 0 & 0 & 0 \\ 0 & \hat{H}_2 & 0 & 0 \\ 0 & 0 & \hat{H}_3 & 0 \\ 0 & 0 & 0 & \hat{H}_4 \end{pmatrix} \begin{pmatrix} \langle\psi_1| \\ \langle\psi_2| \\ \langle\psi_3| \\ \langle\psi_4| \end{pmatrix} \quad 19 \dots\dots\dots 14$$

$$E = \begin{pmatrix} |\psi_1\rangle \\ |\psi_2\rangle \\ |\psi_3\rangle \\ |\psi_4\rangle \end{pmatrix} \begin{pmatrix} \hat{H}_1 & \beta_{12} & \beta_{13} & \beta_{14} \\ \beta_{21} & \hat{H}_2 & \beta_{23} & \beta_{24} \\ \beta_{31} & \beta_{32} & \hat{H}_3 & \beta_{34} \\ \beta_{41} & \beta_{42} & \beta_{43} & \hat{H}_4 \end{pmatrix} \begin{pmatrix} |\psi_1\rangle & |\psi_2\rangle & |\psi_3\rangle & |\psi_4\rangle \end{pmatrix} \quad 20 \dots\dots\dots 15$$

$$\hat{H} = \hat{H}_0 + W(t) = \hat{H}_0 + \mu E(t), \quad 21 \dots\dots\dots 15$$

$$\mu = \begin{pmatrix} 0 & \mu_{01} \\ \mu_{10} & 0 \end{pmatrix}, \quad 22 \dots\dots\dots 15$$

$$\rho^{(1)} = i[\mu(0)E(0)\rho(-\infty) - \rho(-\infty)\mu(0)E(0)] \quad 23 \dots\dots\dots 16$$

$$R^{(1)} = i\langle \mu(t_1)\mu(0)\rho(-\infty) \rangle - \langle \mu(t_1)\rho(-\infty)\mu(0) \rangle. \quad 24 \dots\dots\dots 16$$

$$E_0 = E + E^* = E'(t)e^{-i\omega t} + E'(t)e^{i\omega t}. \quad 25 \dots\dots\dots 16$$

$$P^{(1)}(t) = \int_0^\infty dt_1 [E(t-t_1) + E^*(t-t_1)] R^{(1)}(t_1). \quad 26 \dots\dots\dots 16$$

$$P^{(1)}(t) = Aie^{-i\omega t} \int_0^\infty dt_1 E'(t-t_1) e^{-t_1/T_2} + Aie^{i\omega t} \int_0^\infty dt_1 E'(t-t_1) e^{-t_1/T_2} e^{-2\omega t_1} \\ + Aie^{i\omega t} \int_0^\infty dt_1 E'(t-t_1) e^{-t_1/T_2} + Ai^{-i\omega t} \int_0^\infty dt_1 E'(t-t_1) e^{-t_1/T_2} e^{-2\omega t_1} \quad 27 \dots\dots\dots 16$$

$$i\langle \mu_3 [\mu_2, [\mu_1, [\mu_0, r(-i)]]] \rangle = \\ i\langle \mu_3 \mu_1 \rho(-\infty) \mu_0 \mu_2 \rangle - i\langle \mu_2 \mu_0 \rho(-\infty) \mu_1 \mu_3 \rangle + \Rightarrow R_1 + R_1^* \\ i\langle \mu_3 \mu_2 \rho(-\infty) \mu_0 \mu_1 \rangle - i\langle \mu_1 \mu_0 \rho(-\infty) \mu_2 \mu_3 \rangle + \Rightarrow R_2 + R_2^* \\ i\langle \mu_3 \mu_2 \mu_1 \rho(-\infty) \mu_0 \rangle - i\langle \mu_0 \rho(-\infty) \mu_1 \mu_2 \mu_3 \rangle + \Rightarrow R_3 + R_3^* \quad 28 \dots\dots\dots 17 \\ i\langle \mu_3 \mu_0 \rho(-\infty) \mu_1 \mu_2 \rangle - i\langle \mu_2 \mu_1 \rho(-\infty) \mu_0 \mu_3 \rangle + \Rightarrow R_4 + R_4^* \\ i\langle \mu_3 \mu_2 \mu_1 \mu_0 \rho(-\infty) \rangle - i\langle \rho(-\infty) \mu_0 \mu_1 \mu_2 \mu_3 \rangle + \Rightarrow R_5 + R_5^* \\ i\langle \mu_3 \mu_2 \mu_0 \rho(-\infty) \mu_1 \rangle - i\langle \mu_1 \rho(-\infty) \mu_0 \mu_2 \mu_3 \rangle + \Rightarrow R_6 + R_6^*$$

$$\rho_{10} \propto i\mu_{01} \quad 29 \dots\dots\dots 18$$

$$\rho_{10} \propto i\mu_{01} e^{+i\omega_0 t_1} e^{-t_1/T_2} \quad 30 \dots\dots\dots 18$$

$$\rho_{10} \propto i\mu_{01}^2 e^{+i\omega_0 t_1} e^{-t_1/T_2} \quad 31 \dots\dots\dots 18$$

$$\rho_{11} \propto i\mu_{01}^2 e^{+i\omega_0 t_1} e^{-t_1/T_2} e^{-t_2/T_1} \quad 32 \dots\dots\dots 18$$

$$\rho_{10} \propto i\mu_{01}^3 e^{+i\omega_0 t_1} e^{-t_1/T_2} e^{-t_2/T_1} \quad 33 \dots\dots\dots 18$$

$$\rho_{10} \propto i\mu_{01}^3 e^{+i\omega_0 t_1} e^{-t_1/T_2} e^{-t_2/T_1} e^{-i\omega_0 t_3} e^{-t_3/T_2} \quad 34 \dots\dots\dots 18$$

$$\rho_{10} \propto i\mu_{01}^4 e^{+i\omega_0 t_1} e^{-t_1/T_2} e^{-t_2/T_1} e^{-i\omega_0 t_3} e^{-t_3/T_2} \quad 35 \dots\dots\dots 18$$

$$R_1(t_1, t_2, t_3) \propto i\mu_{01}^4 e^{+i\omega_0 t_1} e^{-t_1/T_2} e^{-t_2/T_1} e^{-i\omega_0 t_3} e^{-t_3/T_2} \quad 36 \dots\dots\dots 18$$

$$\frac{1}{T_2^{(12)}} = \frac{1}{2T_1^{(01)}} + \frac{1}{2T_2^{(12)}} + \frac{1}{T_2^*} = \frac{3}{2T_1^{(01)}} + \frac{1}{T_2^*} \quad 37 \dots\dots\dots 19$$

$$\rho(-\infty) \quad 38 \dots\dots\dots 20$$

$$\rho(-\infty)\mu_o \quad 39 \dots\dots\dots 20$$

$$\mu_1\rho(-\infty)\mu_o \quad 40 \dots\dots\dots 20$$

$$\mu_1\rho(-\infty)\mu_o\mu_2 \quad 41 \dots\dots\dots 20$$

$$\mu_3\mu_1\rho(-\infty)\mu_o\mu_2 \quad 42 \dots\dots\dots 20$$

$$P^{(3)}(t_1, t_2, t_3) \propto \int_0^\infty dt_3 \int_0^\infty dt_2 \int_0^\infty dt_1 \sum_n R_n(t_1, t_2, t_3) \quad 43 \dots\dots\dots 21$$

$$\cdot E_3(t-t_3) E_2(t-t_3-t_2) E_1(t-t_3-t_2-t_1)$$

$$E = e^{-i\omega t + i\mathbf{k}\mathbf{r} + \phi} \quad 44 \dots\dots\dots 24$$

$$\Theta = \frac{a^2 - b^2}{a^2 + b^2} \quad m = \frac{a}{b} \quad 45 \dots\dots\dots 28$$

$$\beta_{weak} = -4\Delta \frac{\beta^2}{(\hbar\omega_2 - \hbar\omega_1)^2} \quad 46 \dots\dots\dots 29$$

$$f = ae^{\frac{-t}{\tau}} + c \quad 47 \dots\dots\dots 37$$

$$H = \begin{pmatrix} \varepsilon & \beta_{12} & \beta_{13} & \beta_{14} \\ \beta_{12} & \varepsilon & \beta_{14} & \beta_{13} \\ \beta_{13} & \beta_{14} & \varepsilon & \beta_{12} \\ \beta_{14} & \beta_{13} & \beta_{12} & \varepsilon \end{pmatrix}, \quad 48 \dots\dots\dots 47$$

$$\beta_{ij} = \frac{1}{4\pi\varepsilon_0} \left[ \frac{\bar{\mu}_i \cdot \bar{\mu}_j}{r_{ij}^3} - 3 \frac{(\bar{r}_{ij} \cdot \bar{\mu}_i)(\bar{r}_{ij} \cdot \bar{\mu}_j)}{r_{ij}^5} \right], \quad 49 \dots\dots\dots 47$$

$$-\frac{i}{\hbar} \frac{\partial}{\partial t} |\psi\rangle = \hat{H} |\psi\rangle \quad 50 \dots\dots\dots 50$$

$$\frac{i}{\hbar} \frac{\partial}{\partial t} \langle\psi| = \langle\psi| \hat{H}^* \quad 51i \dots\dots\dots 50$$

$$\rho = \sum_i p_i |\psi_i\rangle \langle\psi_i| \quad 52 \dots\dots\dots 50$$

$$\begin{aligned} -\frac{i}{\hbar} \rho &= \sum_i p_i |\psi_i\rangle \langle\psi_i| \\ &= \sum_i p_i |\psi_i\rangle \frac{\partial}{\partial t} \langle\psi_i| + \sum_i p_i \left( \frac{\partial}{\partial t} \right) |\psi_i\rangle + \sum_i \left( \frac{\partial}{\partial t} p_i \right) |\psi_i\rangle \langle\psi_i| \end{aligned} \quad 53 \dots\dots\dots 50$$

$$\begin{aligned} -\frac{i}{\hbar} \frac{\partial}{\partial t} \rho &= -\sum_i p_i |\psi_i\rangle \langle\psi_i| \hat{H}^* + \sum_i p_i \hat{H} |\psi_i\rangle \langle\psi_i| + \sum_i \left( \frac{\partial}{\partial t} p_i \right) |\psi_i\rangle \langle\psi_i| \\ &= -\rho \hat{H}^* + \hat{H} \rho + \sum_i \left( \frac{\partial}{\partial t} p_i \right) |\psi_i\rangle \langle\psi_i| \end{aligned} \quad 54 \dots\dots\dots 51$$

$$-\frac{i}{\hbar} \frac{\partial}{\partial t} \rho = [\hat{H}, \rho] + \sum_i \left( \frac{\partial}{\partial t} p_i \right) |\psi_i\rangle \langle\psi_i| \quad 55 \dots\dots\dots 51$$

$$R_1(t_1, t_2, t_3) \propto i\mu_{01}^4 e^{+i\omega_0 t_1} e^{-t_1/T_2} e^{-t_2/T_1} e^{-i\omega_0 t_3} e^{-t_3/T_2} \quad 56 \dots\dots\dots 52$$

$$R_2(t_1, t_2, t_3) \propto i\mu_{01}^4 e^{+i\omega_0 t_1} e^{-t_1/T_2} e^{-t_2/T_1} e^{-i\omega_0 t_3} e^{-t_3/T_2} \quad 57 \dots\dots\dots 52$$

$$R_3(t_1, t_2, t_3) \propto -i\mu_{01}^2 \mu_{12}^2 e^{+i\omega_0 t_1} e^{-t_1/T_2^{(01)}} e^{-t_2/T_1} e^{-i\omega_0 t_3} e^{-t_3/T_2^{(12)}} \quad 58 \dots\dots\dots 52$$



$R_4(t_1, t_2, t_3) \propto i\mu_{01}^4 e^{-i\omega_0 t_1} e^{-t_1/T_2} e^{-t_2/T_1} e^{-i\omega_0 t_3} e^{-t_3/T_2}$	59.....	52
$R_5(t_1, t_2, t_3) \propto i\mu_{01}^4 e^{-i\omega_0 t_1} e^{-t_1/T_2} e^{-t_2/T_1} e^{-i\omega_0 t_3} e^{-t_3/T_2}$	60.....	52
$R_6(t_1, t_2, t_3) \propto -i\mu_{01}^2 \mu_{12}^2 e^{-i\omega_0 t_1} e^{-t_1/T_2^{(01)}} e^{-t_2/T_1} e^{-i\omega_0 t_3} e^{-t_3/T_2^{(12)}}$	61.....	52
$\mathfrak{F}_t[e^{-2\pi\omega_0 t}] = \frac{1}{\pi} \frac{\omega_0}{\omega^2 - \omega_0^2}$	62.....	55
$\mathfrak{F}_t[e^{-2\pi\omega_0 t}] = \sqrt{2\pi} \delta(2i\omega_0 + \omega)$	63.....	56
$\mathfrak{F}_t\left[\frac{1}{\sigma\sqrt{2\pi}} e^{-\frac{t^2}{2\sigma^2}}\right] = \frac{1}{\sqrt{2\pi}} e^{-\frac{\omega^2\sigma^2}{2}}$	64.....	56

## **PREFACE**

The author would like to thank Dr. Sean Garrett-Roe, Zhe Ren, Fan Yang, Tom Brinzer, and Dr. Samrat Dutta for their unfailing support, and to Dr. Sunil Saxena and Dr. Daniel Lambrecht for their assistance. Special thanks also go to Peter Hamm and Martin Zanni for making the theory and practice of 2D IR spectroscopy accessible to the masses.

## 1.0 INTRODUCTION

Nature, in its pursuit of efficiency, reuses successful structures over and over. Consequently, the study of a few iterated motifs can broaden our knowledge of a wide span of different biological systems. One of these recurring structures is the EF-hand  $\text{Ca}^{2+}$ -binding motif is ubiquitous in biological systems, accounting for over 3000 entries in the NCBI Reference Sequences Data Bank.

This diversity is indicative of the wide variety of essential signaling roles that  $\text{Ca}^{2+}$  plays a throughout the life of a cell<sup>1,2,3</sup>. The various EF-hand structures have much in common. The classical EF-hand assembly consists of a 12-residue loop (Figure 1) sandwiched between two  $\alpha$ -helices<sup>4</sup>. The  $\text{Ca}^{2+}$  is ligated by seven carbonyl or carboxyl oxygen atoms in a pentagonal bipyramidal structure, the glutamate forming the only bidentate ligand<sup>5</sup>. The pentagonal bipyramidal structure for binding  $\text{Ca}^{2+}$  is conserved across wide primary structure variations, even when they require significant rearrangement.

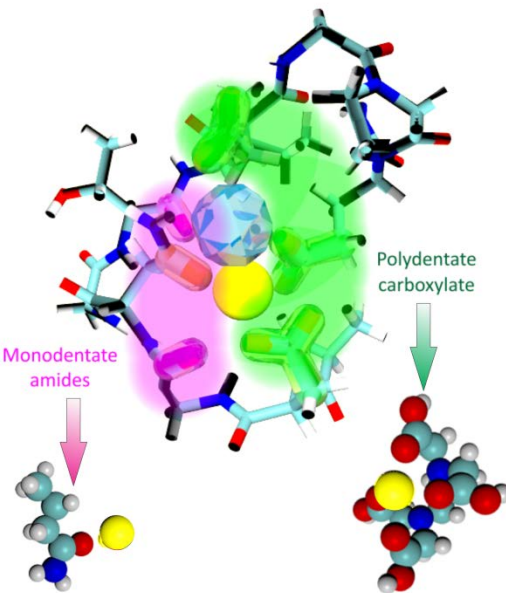


**Figure 1. Detail of the EF-hand binding loop showing detail side-chain carboxylate and backbone and side-chain amide ligands**

A canonical EF-hand structure is represented by that of a human calmodulin (Figure 1). The ligands fall into two general categories: a polydentate carboxylate configuration (green), and various configurations of secondary backbone amides (pink), and side-chain amides (orange) of asparagine and glutamine. A third binding configuration can be assigned to a characteristic water bridge, shown here as a blue icosahedron. Variations in arrangement and identity of ligands in the primary sequence lead to binding affinities that vary by a factor of more than  $10^6$  and which exhibit striking variations in ion selectivity.

X-ray diffraction and NMR studies have yielded static conformational information about both the apo (unbound) and holo (bound) states, and while NMR has returned a limited amount of knowledge about dynamics, its time resolution is too slow to track fast dynamics.

2D-IR spectroscopy, on the other hand, has the time resolution to probe dynamics on the sub-picosecond scale. As the vibrational dynamics of both amides and carboxylates are sensitive to their environment, they can inspect the process of ion binding. Because of the wide application of EF-hand structures, the diversity of unanswered questions, and the comparative simplicity of appropriate models, they are an excellent starting point for exploring the utility of 2D-IR spectroscopy as an analytical tool for such systems.

For this study, butyramide was chosen as a model of amides and EDTA as a model of the polycarboxylate structure. These relatively simple models compose an access point to the study of the complete EF-hand motif, and immediately suggest several avenues of inquiry.

What is the butyramide on/off rate? The weak binding measured by Cremer, et al. <sup>6</sup>, suggest that it is a fast process with the barrier dominated by solvent dynamics. The timescale of hydrogen reorganization in water is on the scale of  $1.5 \text{ ps}^7$  and the timescale of butyramide-ion

associations can be similarly determined by 2D IR spectroscopy. The activation energy of this transition can be calculated from temperature-dependence studies through Arrhenius plots.

What is the mechanism of the blue-shifted butyramide peak? In other words, is the change in carbonyl bond strength a consequence of electrostatic polarization or charge transfer? As charge transfer is known to be the dominant factor in similar systems<sup>8,9</sup>, it is likely that butyramide-ion binding follows the same dynamics. Distinguishing between the two mechanisms is vital because they have different effects on bond strength and therefore on changes to the IR spectrum.

This is easily illustrated using carboxylate as shown in Figure 2. The carboxylate ion has a negative charge, which occupies the  $\pi^*$  antibonding orbital. Charge transfer out of the carboxylate system therefore reduces the antibonding character, strengthening the overall bond.

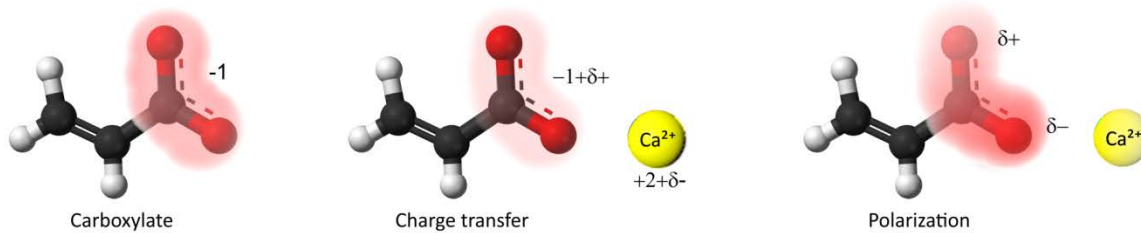


**Figure 2. Representation of charge transfer vs. polarization**

This is reflected in IR as a blue shift of the peak. Polarization, on the other hand, shifts charge from one end of the carboxylate system, effectively strengthening one side and weakening the other. The effect of this on the IR spectrum is less clear-cut

What is the nature of the slight red shift of the butyramide-D<sub>2</sub>O peak with increasing concentration of divalent metal ions? This is tentatively explained by Cremer, et al. as either an effect of the ion hydration shell, or the changing dielectric constant of water. The latter is problematic because monovalent ions also alter the dielectric constant, and Cremer's own data

shows no such shift with NaCl. Likewise, one would expect hydration shell effects from monovalent cations as well.

Of the two ions, the hydration shell of  $\text{Mg}^{2+}$  has a sharper radial distribution function<sup>10</sup> leading to a higher charge density ( $21.2$  vs  $17.9 \Delta\text{V cm}^{-3} \text{ mol}^{-1}$ ) than for calcium<sup>11</sup>. Regardless of the mechanism for the blue shift, one would expect that  $\text{Mg}^{2+}$ 's higher charge density or larger hydration shell to have a different effect than calcium on the immediate environment leading to different IR responses. However, Cremer reports no difference between calcium and magnesium. I offer an alternative hypothesis based on exchange dynamics that will be elaborated upon in the discussion. 2D-IR is uniquely equipped to probe this possibility, which speaks to the fundamental dynamics of amide-ion binding.

Is there a difference between the behavior of backbone and side-chain amides? Backbone amides are secondary amides and those in glutamine and asparagine are primary amides. Secondary amides tend to be stiffer and show the amide I band at about 10 wavenumbers higher than primary amides. My current studies involve butyramide, which is a primary amide and therefore more representative of a side-chain amide than a backbone amide. A secondary amide such as N-methylacetamide will also be studied. Any significant difference between the binding dynamics of the two may signal a difference of their roles in EF-hand. Also, the greater conformational freedom of side-chain amides may be significant.

Most of these questions also need to be answered for EDTA-ion complexes.

One of the variables in EF-hand binding is the selectivity for  $\text{Ca}^{2+}$  over  $\text{Mg}^{2+}$ . As both ions are present in biological systems, and as  $\text{Mg}^{2+}$  competition has been implicated in disease<sup>12</sup> and connected with calcium-signaling modulation<sup>13</sup>, studies will be carried out with both ions.

One variable that should be of interest is the smaller ionic radius of  $\text{Mg}^{2+}$ . Molecular simulations can demonstrate the impact this has on bound geometry, some of which can be confirmed with polarization studies to measure the relative angles of oscillators. The higher field gradient and larger hydration shell of  $\text{Mg}^{2+}$  may play a role. Again, molecular simulation can produce insight, and hydration shell dynamics have already been studied using 2D-IR spectroscopy<sup>14</sup> using techniques directly transferable to this study. Magnesium's lighter mass unlikely has any bearing on static configuration but may play a role in dynamics.

The remainder of this paper will summarize the theory of how 2D IR spectroscopy works and how it can help answer these questions. That will be followed by the results of experimentation so far.

## 2.0 THEORY

### 2.1.1 Describing Molecular Vibrations

#### 2.1.1.1 Basic Oscillator Models

Infrared spectroscopy is a tool of choice for probing molecular dynamics because the frequencies of molecular vibrations correlate with those of infrared radiation. 2D-infrared spectroscopy offers the additional advantage over other tools such as NMR spectroscopy in providing resolution at the sub-picosecond time scale. To understand the role of infrared spectroscopy, it is first necessary to understand molecular vibrations and the interaction of matter and radiation.

Conventional Newtonian mechanics are intractable for problems of any complexity, and although Lagrangian dynamics fulfill an important role where relativistic considerations become significant, is the Hamiltonian formulation,  $\hat{H} = \hat{T} + \hat{V}$ , that is generally most useful in quantum mechanics. It possesses features that make it convenient, particularly that it readily describes the time evolution of a system, and that it yields a direct readout of total system energy, probably the most single valuable parameter. Hamiltonians are easily expressed using formulations for kinetic and potential energy, taking care that the kinetic energy portion is expressed using the quantum mechanical momentum operator  $\hat{p} = -i\hbar\nabla$  instead of the more familiar velocity notation. It is the Hamiltonian that yields the familiar form of the time-independent Schrödinger equation:



$$\hat{H}|\psi\rangle = E|\psi\rangle \quad 1$$

The potential energy well of an interatomic bond is modeled accurately by the Morse potential:

$$V(r) = D_e \left(1 - e^{-a(r-r_e)}\right)^2 \quad 2$$

where  $r$  is the distance between atoms,  $r_e$  is the equilibrium distance,  $a$  is a parameter controlling the well width, and  $D_e$  is the dissociation energy as measured from the bottom of the well.

Although the Schrödinger equation for the Morse potential can be solved exactly, the solution is complex and computationally difficult. It is therefore common practice to use a simple harmonic oscillator model (Figure 3,

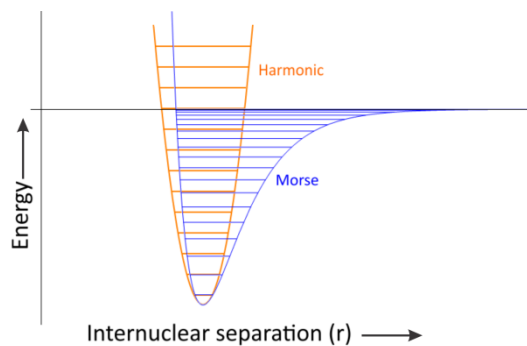


**Figure 3:** Comparison of the Morse potential with a harmonic oscillator.

orange) as an approximation. The approximation is quite good near the bottom of the potential well, and since most infrared spectroscopy experiments deal only with the lowest three energy states, the approximation is not unreasonable. The Hamiltonian is

$$\hat{H} = \frac{\hat{p}^2}{2m} + \frac{1}{2}m\omega^2\hat{x}^2 = -\hbar\frac{\partial^2}{dx^2} + \frac{1}{2}m\omega^2\hat{x}^2 \quad 3$$

yielding equally spaced energy levels of

$$E_v = \hbar\omega\left(v + \frac{1}{2}\right). \quad 4$$

The harmonic oscillator approximation also allows us to express  $\omega$  classically in terms of a “spring” constant,  $k$ , and reduced mass,  $\mu$ :

$$\omega = \sqrt{\frac{k}{\mu}} \quad 5$$

As useful as the harmonic oscillator is, it is important to remember that it is just an approximation. The deviation of the real potential energy environment from the harmonic oscillator, termed anharmonicity, is ultimately responsible for the fact that infrared spectroscopy works at all, and that certain faint transitions forbidden in the harmonic case can, in fact, occur. It is also important to note that the energy levels of a harmonic oscillator extend, mathematically, to infinity, but that a Morse potential – and real bonds – have a point above which the system is unbound and the notion of discrete energy levels becomes meaningless.

Up until this point, we have assumed that the only potential energy present is that of the Morse potential or its approximation, the harmonic oscillator potential. But except in the case of a sufficiently rarefied gas phase, interactions with other molecules must also be considered.

As infrared activity requires a non-zero transition dipole moment, it follows that there must exist dipoles. They appear in the form of polar bonds, and those with a strong transition dipole moment such as carbonyl groups make excellent chromophores for infrared studies. They allow the probing of the immediate environment, because the interaction between that dipole and other sources of

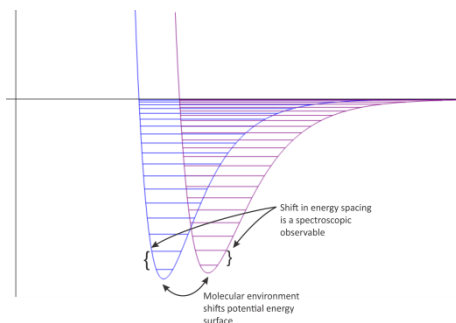


**Figure 4: The widening of a potential well by external forces compresses the energy levels.**

electric potential (charges, other dipoles, etc.) modify the energy environment from that of the pure Morse potential (Figure 4). An attractive force on, let's say, the oxygen of the carbonyl or the hydrogen of an amine, will “stretch” the bond, weaken it, and compress the energy levels between adjacent states. It is this compression of energy levels that directly corresponds to the shift in infrared observables that forms the basis of IR spectroscopy as an exploratory probe.

Hence, we appear forced to choose between a harmonic oscillator model, which is inaccurate except very near the ground state, and the Morse potential model, which is accurate but more difficult to work with. In many areas of physics and chemistry mathematical approximation methods are available to ease the burden. Among these is perturbation theory, widely used in spectroscopy. In modeling a complex Hamiltonian, we start with an easy one, such as the harmonic oscillator, and add a small correction (the perturbation) to get closer to the real answer:

$$\hat{H} = \hat{H}_0 + \hat{H}' \quad \mathbf{6}$$

The Morse potential proves to be very cooperative in this regard. The energy levels for an oscillator in the Morse potential are given by

$$E = \hbar\omega\left(v + \frac{1}{2}\right) - \hbar\omega\chi\left(v + \frac{1}{2}\right)^2, \quad \mathbf{7}$$

where  $\chi$  is the anharmonicity term. This expression is already in the form of a perturbative expansion because the first term is that of the harmonic oscillator and the second is a second-order term in the same variable. Thus, we can use the simple harmonic oscillator model for general work and add the second-order anharmonicity term when it is required for accuracy.

We know that in the absence of any external perturbing potential fields, the individual vibrational solutions are given by the time-dependent Schrödinger equation:

$$i\hbar\frac{\partial}{\partial t}|\psi\rangle = E|\psi\rangle, \quad \mathbf{8}$$

where  $|\psi\rangle$  represents the wave function in Dirac notation, also called *bra-ket* notation. The symbol used here is the *ket*, effectively a row vector, and its complex conjugate,  $\langle\psi|$ , is the *bra*,

effectively a column vector. Using that convention,  $\langle \psi_1 | \psi_2 \rangle$  is the inner product and  $|\psi_1\rangle\langle\psi_2|$  is the outer product.

The time-dependent Schrödinger equation yields the set of solutions:

$$|\psi\rangle = \sum_n c_n e^{-iE_n t/\hbar} |n\rangle. \quad 9$$

This expression confirms what we already knew about wave functions and, more generally, differential equations: if  $\psi_1$  and  $\psi_2$  are solutions, then so must be any linear combination of them.

The existence of an exponential with an imaginary exponent suggests an oscillation, but if we think of the classical illustration of the ball-and-spring molecular bond falling into resonance with a matching incoming wave, we find that it fails to explain spectroscopic processes very

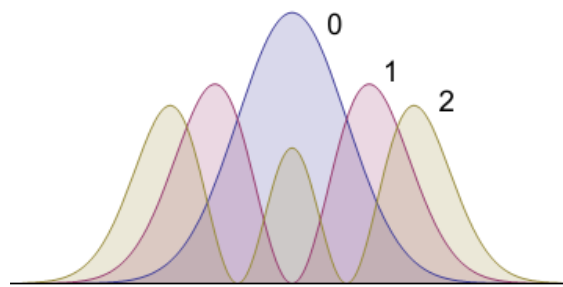


**Figure 5:** The first three probability waves of the quantum harmonic oscillator.

deeply. Figure 5 shows the probability density of the first three vibration numbers, those of concern to most two-dimensional infrared spectroscopy. Each curve represents the probability that the atoms of the oscillator will have a particular separation, but it is impossible to say with any certainty that anything is moving in the classical sense. We must look deeper to discover the oscillation that the radiation wave couples to.

### 2.1.1.2 The Density Matrix and Ensembles

There are an infinite number of potential superposition states for any oscillator involving any number of eigenstates. However, we restrict ourselves to superposition states that are

spectroscopically interesting and which have a measurable population. The most fundamental of these is that between states  $|0\rangle$  and  $|1\rangle$ :

$$\psi_{01} = c_0 e^{-iE_0 t/\hbar} + c_1 e^{-iE_1 t/\hbar} = \begin{pmatrix} c_0 e^{-iE_0 t/\hbar} \\ c_1 e^{-iE_1 t/\hbar} \end{pmatrix} \quad 10$$

To describe the self-interaction, we introduce the *density matrix*, which outer product of the wavefunction with its complex conjugate:

$$\begin{aligned} \rho = |\psi\rangle\langle\psi| &= \begin{pmatrix} c_0 e^{-iE_0 t/\hbar} |0\rangle \\ c_1 e^{-iE_1 t/\hbar} |0\rangle \end{pmatrix} \begin{pmatrix} c_0^* e^{iE_0 t/\hbar} \langle 1| & c_1^* e^{iE_1 t/\hbar} \langle 1| \end{pmatrix} \\ &= \begin{pmatrix} c_0^2 & c_0 c_1^* e^{i(E_1 - E_2)t/\hbar} \\ c_1 c_0^* e^{i(E_2 - E_1)t/\hbar} & c_1^2 \end{pmatrix} \\ &= \begin{pmatrix} c_0^2 & c_0 c_1^* e^{i\omega_0 t} \\ c_0^* c_1 e^{-i\omega_0 t} & c_1^2 \end{pmatrix} \end{aligned} \quad 11$$

The last line simplifies the expression by replacing the difference in energy between the two states with the angular frequency corresponding to that difference. If the wavefunction were normalized, we see that the sum of the diagonal terms (the trace) must equal 1 for any single oscillator. The off-diagonal terms are the ones that introduce the oscillatory process for an external field to interact with.

Such a state is called a *coherent state*, or more simply, a coherence, and appears when the wavefunction is a superposition of more than one eigenstates. The term coherence generally refers to two periodic waves with identical frequency and phase, and applies here to the off-diagonal terms. The alternative is a system that is composed of a single eigenfunction, called a *population state*, where the density matrix reduces to

$$|0\rangle\langle 0| = \begin{pmatrix} 1 & 0 \\ 0 & 0 \end{pmatrix}, \quad |1\rangle\langle 1| = \begin{pmatrix} 0 & 0 \\ 0 & 1 \end{pmatrix}. \quad 12$$

Since one of the coefficients is 0, there can be no oscillatory off-diagonal terms in the density matrix, and so a population state does not absorb or radiate.

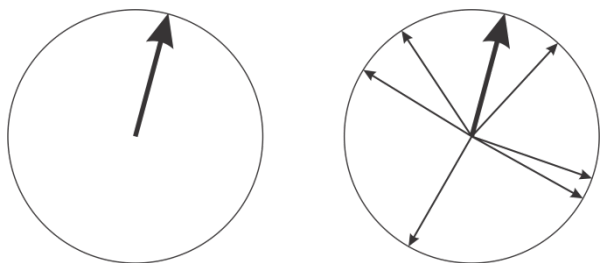


**Figure 6: Illustration of a pure state and a mixed state with the same net vector.**

Although the density matrix was introduced for a single oscillator, it is an essential tool for describing an ensemble of molecules. A state that can be described as a linear combination of eigenstates is known as a *pure state*. It can be thought of as a single vector of

length 1 in the space of eigenstates. Over an ensemble, it is possible to find a sum of states adding to some arbitrary pure state (Figure 6). Such a state is called a *mixed state*. The mixed state shown here has a length of 1 but it does not need to.

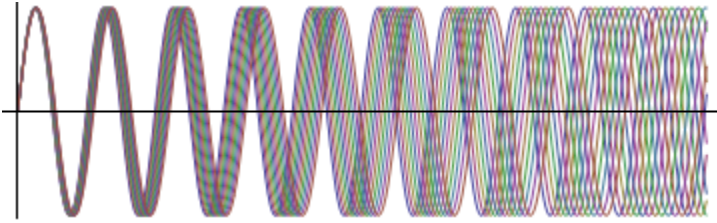
A single oscillator cannot lose its other than by the shift of all of its energy to a single eigenstate:

$$\begin{pmatrix} \frac{1}{2} & -\frac{i}{2}e^{i\omega_0 t} \\ \frac{i}{2}e^{-i\omega_0 t} & \frac{1}{2} \end{pmatrix} \rightarrow \begin{pmatrix} 1 & 0 \\ 0 & 0 \end{pmatrix} \quad 13$$

Because the off-diagonal terms are cross products, they can only be non-zero if the coefficients for both eigenstates are non-zero. A mixed state presents another situation. Because it represents an ensemble, it is possible that individual systems will relax to one or the other eigenstate, leaving both of them partially occupied:

$$\begin{pmatrix} \frac{1}{2} & -\frac{i}{2}e^{i\omega_0 t} \\ \frac{i}{2}e^{-i\omega_0 t} & \frac{1}{2} \end{pmatrix} \rightarrow \begin{pmatrix} \frac{1}{2} & 0 \\ 0 & \frac{1}{2} \end{pmatrix} \quad 14$$

There is a second method by what a mixed state can lose coherence. Especially in the condensed phase, the various oscillators composing the state are in slightly different potential energy environments. So although they start out in phase, that phase synchronization is lost as



time progresses (**Figure 7** Dephasing because of variations in energy environment)..The average of the oscillatory terms trends toward zero.

**Figure 7 Dephasing because of variations in energy environment**

Although there is a more rigorous explanation of dephasing (see Appendix) and more sophisticated

models are available, it is common to represent dephasing by adding an exponential decay to the off-diagonal terms in the density matrix:

$$\rho^{(1)} = \begin{pmatrix} c_0^2 & c_0 c_1^* e^{i\omega_0 t} e^{t/T_2} \\ c_0^* c_1 e^{-it\omega_0} e^{t/T_2} & c_1^2 \end{pmatrix} \quad 15$$

where  $T_2$  is the dephasing time. There are two components to this process, the pure dephasing time  $T_2^*$ , which includes only the actual dephasing process described about, and  $T_1$ , which is the population relaxation time. As population relaxation drives more oscillators toward the ground state, the off-diagonal terms must also diminish because they come about as cross products. The three time constants are related by

$$\frac{1}{T_2} = \frac{1}{2T_1} + \frac{1}{T_2^*}. \quad 16$$

The superscript assigned to  $\rho^{(1)}$  in Equation 15 designates that this is the first-order expansion of the complete density matrix. In real-world applications, only a small percentage of

oscillators are actually excited, so most of them remain in the ground state, and some energy goes in to higher terms of the density matrix expansion. The complete density matrix is more accurately described by

$$\rho = \rho^{(0)} + \rho^{(1)} + \dots = \begin{pmatrix} 1 & 0 \\ 0 & 0 \end{pmatrix} + \begin{pmatrix} c_0^2 & -c_0 c_1^* e^{i\omega_0 t} \\ c_0^* c_1 e^{-i\omega_0 t} & c_1^2 \end{pmatrix} + \dots \quad 17$$

In spectroscopy,  $\rho^{(0)}$  is of little interest, and higher terms are generally small, so we restrict our focus to  $\rho^{(1)}$ . Nevertheless, it is important to recognize the existence of higher order terms, as they explain what would otherwise look like the disappearance of energy when we consider absorption.

### 2.1.1.3 Vibrational Excitons

Up until this point, we have considered uncoupled oscillators, that is, oscillators that do not transfer energy between them. This transfer results in new distributed vibrational modes that must be analyzed as a whole. We know from quantum mechanics that the expectation value for an observable,  $A$ , is given by:

$$A = \langle \psi | \hat{A} | \psi \rangle \quad 18$$

With four discrete uncoupled oscillators, we can treat them individually as shown here in matrix form:

$$E = \begin{pmatrix} |\psi_1\rangle \\ |\psi_2\rangle \\ |\psi_3\rangle \\ |\psi_4\rangle \end{pmatrix} \begin{pmatrix} \hat{H}_1 & 0 & 0 & 0 \\ 0 & \hat{H}_2 & 0 & 0 \\ 0 & 0 & \hat{H}_3 & 0 \\ 0 & 0 & 0 & \hat{H}_4 \end{pmatrix} \begin{pmatrix} |\psi_1\rangle & |\psi_2\rangle & |\psi_3\rangle & |\psi_4\rangle \end{pmatrix} \quad 19$$

However, when the oscillators are coupled, we must add energy terms in the off-diagonals to represent that coupling:



$$E = \begin{pmatrix} |\psi_1\rangle \\ |\psi_2\rangle \\ |\psi_3\rangle \\ |\psi_4\rangle \end{pmatrix} \begin{pmatrix} \hat{H}_1 & \beta_{12} & \beta_{13} & \beta_{14} \\ \beta_{21} & \hat{H}_2 & \beta_{23} & \beta_{24} \\ \beta_{31} & \beta_{32} & \hat{H}_3 & \beta_{34} \\ \beta_{41} & \beta_{42} & \beta_{43} & \hat{H}_4 \end{pmatrix} \begin{pmatrix} |\psi_1\rangle & |\psi_2\rangle & |\psi_3\rangle & |\psi_4\rangle \end{pmatrix} \quad 20$$

[More about the exciton Hamiltonians]

## 2.1.2 Interaction with Radiation

### 2.1.2.1 The Response Function

Now that we have a basic understanding of quantum molecular vibrations and a language with which to discuss entire ensembles, we can approach of interaction of infrared radiation with matter.

Under the influence of an external field, the native Hamiltonian is modified. Again, we treat this as a perturbation

$$\hat{H} = \hat{H}_0 + W(t) = \hat{H}_0 + \mu E(t), \quad 21$$

where  $\mu$  is the transition dipole moment and  $E(t)$  is the electric field, which we consider only as a scalar field at this point. Because the transition dipole moment generates off-diagonal terms in the density matrix, it must be of the form

$$\mu = \begin{pmatrix} 0 & \mu_{01} \\ \mu_{10} & 0 \end{pmatrix}, \quad 22$$

though both terms are generally considered identical.

In order to be a complete interaction, the dipole perturbation must be applied to both sides of the density matrix, i.e., to both the bra and the ket. As shown by the Liouville-von Newman equation (see Appendix I for derivation), this interaction appears as a commutator:

$$\rho^{(1)} = i[\mu(0)E(0)\rho(-\infty) - \rho(-\infty)\mu(0)E(0)] \quad 23$$

For the macroscopic behavior of an ensemble, we must consider the expectation value, which is equal to the trace. The response function is now defined as the interaction of the density matrix with a second dipole:

$$R^{(1)} = i\langle \mu(t_1)\mu(0)\rho(-\infty) \rangle - \langle \mu(t_1)\rho(-\infty)\mu(0) \rangle. \quad 24$$

### 2.1.2.2 Polarization

With some simplifying assumptions, the macroscopic polarization in response to a pulse is simply the convolution of the pulse with the first-order response function, but we need to use a more sophisticated model of the pulse electric field. We continue overlook that the field is a vector until section ???, but now we must apply the knowledge that the real observable aspect of the electric field wave consists of two components that are complex conjugates of each other:

$$E_0 = E + E^* = E'(t)e^{-i\omega t} + E'(t)e^{i\omega t}. \quad 25$$

Therefore, the convolution can be written as

$$P^{(1)}(t) = \int_0^\infty dt_1 [E(t-t_1) + E^*(t-t_1)] R^{(1)}(t_1). \quad 26$$

However, as the response function also has two terms deriving from the commutator, the integral becomes

$$\begin{aligned} P^{(1)}(t) = & Aie^{-i\omega t} \int_0^\infty dt_1 E'(t-t_1) e^{-t_1/T_2} + Aie^{i\omega t} \int_0^\infty dt_1 E'(t-t_1) e^{-t_1/T_2} e^{-2\omega t_1} \\ & + Aie^{i\omega t} \int_0^\infty dt_1 E'(t-t_1) e^{-t_1/T_2} + Ai^{-i\omega t} \int_0^\infty dt_1 E'(t-t_1) e^{-t_1/T_2} e^{-2\omega t_1} \end{aligned} \quad 27$$

The left-hand integrands come from where the factors combine with opposite signs in the exponent and become a relatively slowly varying exponential factor. The integrands on the right

coming from the combination of terms with like signs, contain a rapidly oscillating term, that over the interval of the convolution average to zero. This is called the rotating wave approximation, and immediately cuts in half the number of possibilities we have to consider.

Also, the two remaining terms are complex conjugates of each other, and although both are necessary for physical reality, they contain the same information, and so we need to consider only one of them for the mathematical analysis of response.

Minimizing the number of pathways to consider is important because they grow

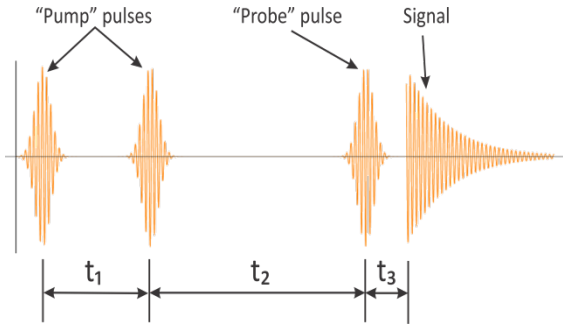


**Figure 8: Timing sequence of a third-order spectroscopy**

explosively. Two-dimensional IR spectroscopy, uses three pulses with four pathways each. Without being able to eliminate a good portion of them, we could be left with  $4^3 = 64$  possible combinations, a lot to work with. A sequence of three pulses requires four nested commutators of their dipole interactions with the prior density matrix, which

expand into four pair of interactions:

$$\begin{aligned}
 & i \left\langle \mu_3 \left[ \mu_2, \left[ \mu_1, \left[ \mu_0, r(-i) \right] \right] \right] \right\rangle = \\
 & i \langle \mu_3 \mu_1 \rho(-\infty) \mu_0 \mu_2 \rangle - i \langle \mu_2 \mu_0 \rho(-\infty) \mu_1 \mu_3 \rangle + \Rightarrow R_1 + R_1^* \\
 & i \langle \mu_3 \mu_2 \rho(-\infty) \mu_0 \mu_1 \rangle - i \langle \mu_1 \mu_0 \rho(-\infty) \mu_2 \mu_3 \rangle + \Rightarrow R_2 + R_2^* \\
 & i \langle \mu_3 \mu_2 \mu_1 \rho(-\infty) \mu_0 \rangle - i \langle \mu_0 \rho(-\infty) \mu_1 \mu_2 \mu_3 \rangle + \Rightarrow R_3 + R_3^* \quad 28 \\
 & i \langle \mu_3 \mu_0 \rho(-\infty) \mu_1 \mu_2 \rangle - i \langle \mu_2 \mu_1 \rho(-\infty) \mu_0 \mu_3 \rangle + \Rightarrow R_4 + R_4^* \\
 & i \langle \mu_3 \mu_2 \mu_1 \mu_0 \rho(-\infty) \rangle - i \langle \rho(-\infty) \mu_0 \mu_1 \mu_2 \mu_3 \rangle + \Rightarrow R_5 + R_5^* \\
 & i \langle \mu_3 \mu_2 \mu_0 \rho(-\infty) \mu_1 \rangle - i \langle \mu_1 \rho(-\infty) \mu_0 \mu_2 \mu_3 \rangle + \Rightarrow R_6 + R_6^*
 \end{aligned}$$

Each pair subsequently leads to a pair of response functions, a response and its complex conjugate.

We go through the steps that take place and explicitly build response function  $R_1$  :

1. We start at the ground population state  $|0\rangle\langle 0|$ .

2. An interaction from the right, elevating the system to a  $|0\rangle\langle 1|$  coherence state:

$$\rho_{10} \propto i\mu_{01} \quad \mathbf{29}$$

3. The system dephases for time  $t_1$  :

$$\rho_{10} \propto i\mu_{01} e^{+i\omega_0 t_1} e^{-t_1/T_2} \quad \mathbf{30}$$

4. At time  $t_1$ , the second pulse interacts from the left, elevating the system to a  $|1\rangle\langle 1|$  population state:

$$\rho_{10} \propto i\mu_{01}^2 e^{+i\omega_0 t_1} e^{-t_1/T_2} \quad \mathbf{31}$$

5. During time period  $t_2$ , the system undergoes population relaxation:

$$\rho_{11} \propto i\mu_{01}^2 e^{+i\omega_0 t_1} e^{-t_1/T_2} e^{-t_2/T_1} \quad \mathbf{32}$$

6. At time  $t = t_1 + t_2$ , the third pulse interacts from the right, reducing the system to a  $|1\rangle\langle 0|$  coherence state. Why it does not elevate it to a  $|1\rangle\langle 2|$  coherence state is related to the rotating wave approximation and will become clearer in the next section.

$$\rho_{10} \propto i\mu_{01}^3 e^{+i\omega_0 t_1} e^{-t_1/T_2} e^{-t_2/T_1} \quad \mathbf{33}$$

7. During time  $t_3$ , the system once again dephases:

$$\rho_{10} \propto i\mu_{01}^3 e^{+i\omega_0 t_1} e^{-t_1/T_2} e^{-t_2/T_1} e^{-i\omega_0 t_3} e^{-t_3/T_2} \quad \mathbf{34}$$

8. Finally, the field interaction occurs from the left, generating the signal field:

$$\rho_{10} \propto i\mu_{01}^4 e^{+i\omega_0 t_1} e^{-t_1/T_2} e^{-t_2/T_1} e^{-i\omega_0 t_3} e^{-t_3/T_2} \quad \mathbf{35}$$

Now we can write the response function:

$$R_1(t_1, t_2, t_3) \propto i\mu_{01}^4 e^{+i\omega_0 t_1} e^{-t_1/T_2} e^{-t_2/T_1} e^{-i\omega_0 t_3} e^{-t_3/T_2} \quad \mathbf{36}$$

The other response functions are generated similarly. Recall that the dephasing  $T_2$  is a combination of pure dephasing  $T_2^*$  and population relaxation  $T_1$ . We can assume that the pure dephasing is the same for both states, but the  $|2\rangle \rightarrow |1\rangle$  population relaxation time accessible via the pathways associated with  $R_3$  and  $R_6$ , is twice as fast as the  $|1\rangle \rightarrow |0\rangle$  relaxation time. Therefore, we must distinguish between  $T_2^{(01)}$  and  $T_2^{(12)}$ . The overall dephasing times are related by

$$\frac{1}{T_2^{(12)}} = \frac{1}{2T_1^{(01)}} + \frac{1}{2T_2^{(12)}} + \frac{1}{T_2^*} = \frac{3}{2T_1^{(01)}} + \frac{1}{T_2^*} \quad 37$$

See Appendix B for a complete list of response functions for a third-order system.

### 2.1.3 Feynman Diagrams and Rephasing

Needless to say, keeping track of all the details of four interactions is a daunting challenge and prone to error. Feynman diagrams serve to both communicate graphically a sequence of interactions, and to help sort out which of those are useful. Named after the physicist Richard Feynman, it is probable that Feynman never used these, but they function the same as his original diagrams in providing a graphical representation of multiple quantum pathways.

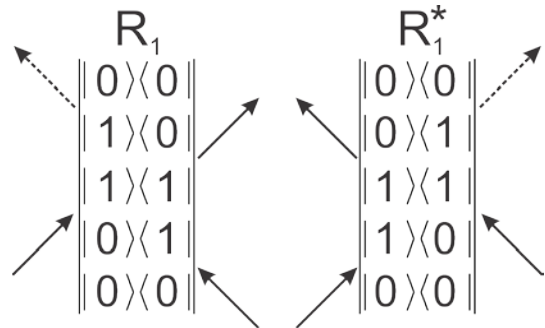


**Figure 9: Feynman diagrams for  $R_1$  and  $R_1^*$  pathways**

**Figure 9:** Feynman diagrams for  $R_1$  and  $R_1^*$  pathways Shows Feynman diagrams for the  $R_1$  and  $R_1^*$  pathways. The states shown between the vertical bars are those occupied in temporal order, with increasing time toward the top. Arrows

indicate field interactions on the ket (left) and bra (right), the direction of the arrow representing either the  $E$  (pointing right) or  $E^*$  (pointing left) portion of the electric field. For a complete list of Feynman diagram rules see Appendix C.

A number of features facilitate work with multiple pathways. First, complex conjugates are mirror images of each other, so that it is easy to identify them. Since they report identical information, we only need to track one of them, and by convention use the form placing the interaction of the signal field (dashed arrow) at the upper left. Second, we see that arrows entering the system raise the state of the bra or ket, and arrows exiting lower the state. This is intuitive. The counter-intuitive propositions, that arrows entering lower the state or exiting raise the state, are those that are excluded by the rotation wave approximation.

Third, Feynman diagrams make it easy to formulate a response function. To illustrate, we build the  $R_1$  interaction from the Feynman diagram.

1. Start with the ground-state density matrix.

$$\rho(-\infty) \quad 38$$

2. Add the  $t_1$  interaction from the right.

$$\rho(-\infty)\mu_o \quad 39$$

3. Add the  $t_2$  interaction from the left.

$$\mu_1\rho(-\infty)\mu_o \quad 40$$

4. Add the  $t_3$  interaction from the right.

$$\mu_1\rho(-\infty)\mu_o\mu_2 \quad 41$$

5. Finally, add the signal interaction from the left.

$$\mu_3\mu_1\rho(-\infty)\mu_o\mu_2 \quad 42$$

We see that this agrees exactly with the interaction obtained by expansion of nested commutators as shown in Equation 29. Construction of response functions is further facilitated by noting that arrows pointing to the right generate coherences that evolve according to  $e^{-i\omega t}$  and those pointing left to  $e^{i\omega t}$ .

Fourth, Feynman diagrams allow us to distinguish rephasing from non-rephasing pathways. Examining a sample of each in **Figure 10**: Rephasing vs non-rephasing pathways, we note that they are identical except for the second coherence state: in the rephasing case they are opposite; in the non-rephasing case, they are identical. In the rephasing case, the

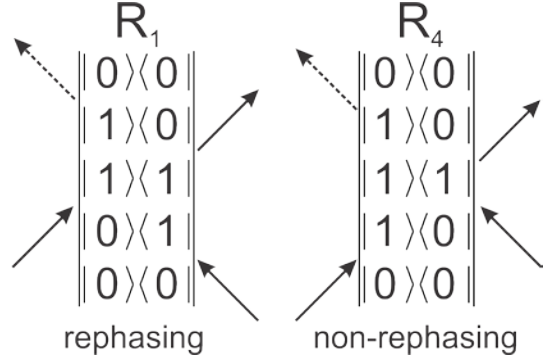


**Figure 10: Rephasing vs non-rephasing pathways**

first coherence is generated by an interaction of the form  $e^{i\omega t}$  and the second by one of the form  $e^{-i\omega t}$ . Consequently, the second coherence state evolves in the opposite direction of the first, reversing dephasing, and eventually generating the photon echo shown in **Figure 8**: Timing sequence of a third-order spectroscopy. In this case, both coherences are generated by an interaction of the form  $e^{-i\omega t}$ , so there is no reversal. Although less intuitive in the case of non-rephasing pathways, both appear at the detector and are needed to construct complete spectroscopic observables.

We are now able to construct a complete representation of the macroscopic third-order polarization:

$$P^{(3)}(t_1, t_2, t_3) \propto \int_0^\infty dt_3 \int_0^\infty dt_2 \int_0^\infty dt_1 \sum_n R_n(t_1, t_2, t_3) \cdot E_3(t-t_3) E_2(t-t_3-t_2) E_1(t-t_3-t_2-t_1) \quad 43$$

## 2.1.4 Implementation

### 2.1.4.1 Overview

It is beyond the scope of this document to present all of the knowledge needed to build a 2D infrared spectrometer, but an overview is necessary to help understand the spectra that come from it.

The premise of 2D Infrared spectroscopy is a plot of input ( $\omega_1$ ) vs output ( $\omega_2$ ) frequencies over the range of interest. The canonical arrangement consists of an ultrafast (100fs) infrared pulse laser, an optical parametric amplifier (OPA) to tune the output of the laser to frequency of the selected chromophore, and the spectrometer itself. The pulses from the OPA are split into four and routed through a series of computer-controlled precision translation stages to adjust the timing between pulses. The first two, corresponding to the pulses at  $t_1$  and  $t_2$  (**Figure 8**: Timing sequence of a third-order spectroscopy are usually called pump pulses. The third is the probe pulse at  $t_3$ , and fourth is a reference pulse, identical to the probe pulse, but passing through the sample in a region not exposed to the pump pulses to establish a baseline for the spectroscopy. The generated signal pulse passes to an infrared spectrometer, in our case 32 channels wide, which directly provides the data for the output axis.

We can assume that the system starts in the  $|0\rangle\langle 0|$  ground state because at room temperature, the difference in energy levels is significantly higher than  $k_B T$ . The first pulse places the system into either a  $|0\rangle\langle 1|$  or  $|1\rangle\langle 0|$  coherence state, and the second puts it into a  $|0\rangle\langle 0|$  or  $|1\rangle\langle 1|$  population state. The time between  $t_1$  and  $t_2$  is referred to as a *coherence time*. The time between  $t_2$  and  $t_3$  is known as a *population time*.



### 2.1.4.2 Generating the $\omega_1$ axis

The coherence time between  $t_1$  and  $t_2$  also generates the  $\omega_1$  axis. A sample of several thousand  $\omega_3$  are recorded against different values of  $\tau_1 = t_2 - t_1$ . The Fourier transform converts the  $\tau_1$  time base to a frequency. While designs exist that actually sweep the frequency, given that pulses at  $t_1$  and  $t_2$  are necessary anyway for third-order spectroscopy, it is often more practical to use this method.

It is easy to say that a Fourier transform converts a time axis to a frequency axis, but the reality is less than intuitive, so a physical picture is helpful. The shape of the laser pulse is approximately Gaussian, and the Fourier transform also inverts the width of a Gaussian pulse, in

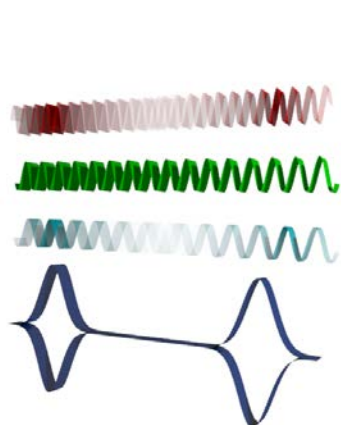


**Figure 11: How timing changes can determine a frequency**

the sense that a narrow pulse in one domain is converted to a wide pulse in the other domain. As the pulse is quite short in the time domain, there must be a wide distribution of frequencies around the center frequency (Section 1.01(a)(i)Appendix D). Mathematically, each of the frequency components is a sine wave of infinite length (Figure 11), the various frequency components of the pulses overlap in time even though the pulses themselves, intuitively, do not. At each value of  $\tau_1$ , there was one frequency (green) within the

range of interest that is in phase across both pulses. Other frequencies (red, blue) are out of phase and attenuated.

During the  $\tau_2 = t_3 - t_2$  population time, the system evolves in ways that are spectroscopically interesting in ways other than during coherence time. Two such general categories are chemical exchange, where an oscillator moves to another chemical environment where its frequency has changed, and relaxation, where energy transfers quantum

mechanically from one system to another. More detailed information appears below in Section 2.1.5.

### 2.1.4.3 Phase matching

Recall that until this point, we have been ignoring the vector nature of the. We still ignore the field polarization for the moment, but apply the direction of travel vector. Instead of the approximation  $e^{-i\omega t}$ , we will use the more complete expression:

$$E = e^{-i\omega t + i\mathbf{k}\mathbf{r} + \phi} \quad 44$$

where  $\mathbf{k}$  is the propagation vector and  $\phi$  is the phase.

Coherence states remember the propagation vector and phase in addition to the frequency. Light has been held “stationary” for up to a minute<sup>15</sup>, orders of magnitude longer than of interest to spectroscopists. Figure 1 shows the wave vectors for a hypothetical three-pulse system.

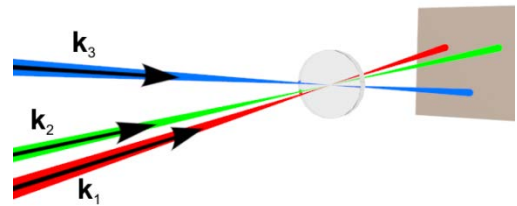


Figure 12: Propagation vectors

However, it is common to use the projection of those factors onto the target plane, and for those we will use the notation  $\vec{k}_1$ ,  $\vec{k}_2$ , and  $\vec{k}_2$ .

Labeling the interaction arrows on a Feynman diagram with the propagation vectors facilitates ??? (Figure 13). Arrows to the right are positive; arrows to the left are negative. The vector sum is then the direction of the emitted signal. Not all pathways can be so easily separated, but many of them can. Note that in the example here, though it is possible to place a detector in the location of each output stream, it is usually more practicable to place a detector at only one location and reverse the timing of the first two pulses to select the pathway needed.

In our instrument, the two pump beams are collinear. Since  $\vec{k}_1 - \vec{k}_2 = 0$ , the output signal is collinear with  $\vec{k}_3$ . This has an important ramification in the next section.

#### 2.1.4.4 The Local Oscillator

There remains but one term to consider, the phase  $\phi$  in the wave. Proper registration requires a phase reference, and this is often provided by another source or by another

portion of the original laser pulse split off for that purpose. Either way, this is referred to as the *local oscillator*. In our

configuration, however, as the pump pulses are collinear and the emitted field in collinear with the probe pulse, the transmitted portion of the probe pulse functions as the local oscillator and is automatically in the correct phase.

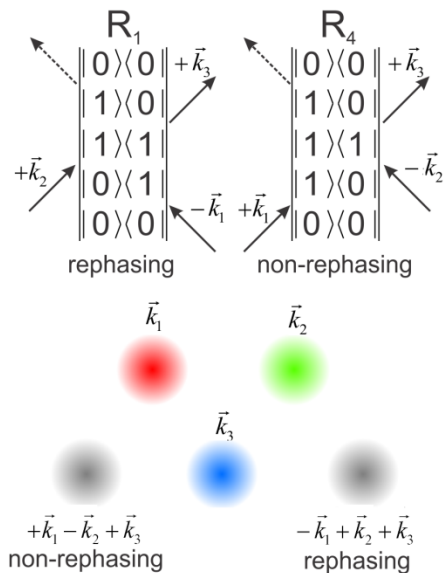


**Figure 13: Phase matching with Feynman Diagrams**

### 2.1.5 Spectroscopic Observables

#### 2.1.5.1 Classical Spectroscopic Processes and Anharmonicity

Certain processes that are indistinguishable under linear IR are distinguishable under 2D IR. We begin that discussion with a semi-classical view of spectroscopy that knows nothing about coherences. Under that view, a process begins when the system absorbs a photon, which raises it from the  $\nu = 0$  state to the  $\nu = 1$  state. Note that the photons in this picture are not the same as the field interactions described in this paper, as herein it requires two field interactions

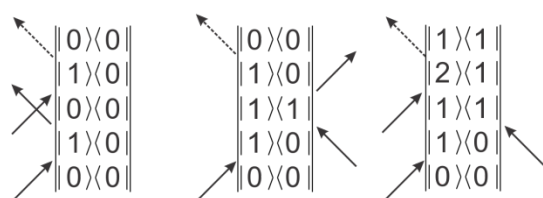
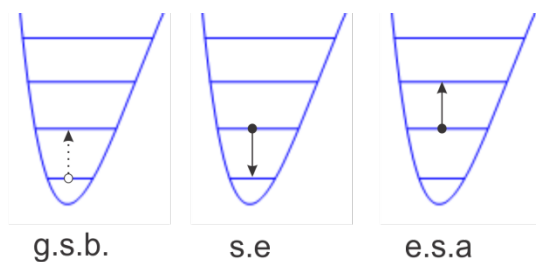


**Figure 14: The three classical spectroscopic processes**

to achieve the  $\nu=1$  state. Once the system is in this state, there are three classical pathways it can take in response to a second photon (Figure 14). The equivalent Feynman diagrams are shown.

Ground-state bleach (g.s.b.) is the absence of an excitation that might have happened had the population of oscillators in the ground state not been reduced by the first photon. This appears at the detector as increased signal and therefore interpreted as a decrease in absorption.

Stimulated emission (s.e.) occurs when the second photon couples the excited oscillator back to the ground state. This also appears as an increased signal or decrease in absorption. Excited-state absorption (e.s.a.) occurs when the system absorbs a second photon and is elevated to the  $\nu=2$  state. This is a decrease in signal and in increase in absorption.

These processes appear as two spots on a 2D IR spectrum (Figure 15). Ground-state bleach and stimulated emission combine to form the red spot on the diagonal. Excited-state absorption forms the blue spot. By convention, the red is considered positive and the blue negative. The offset ( $\Delta$ ) between them

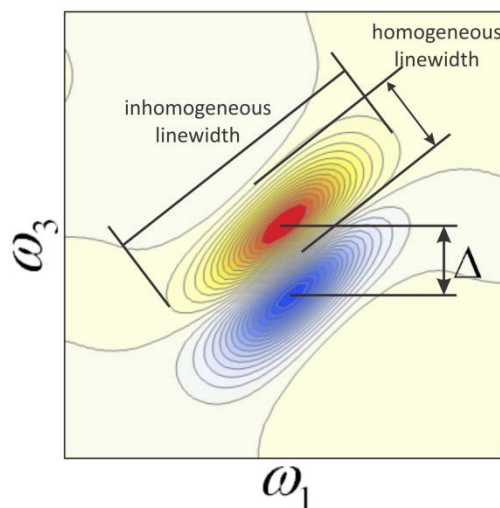


**Figure 15. Essentials of a 2D IR spectrum, showing anharmonicity.**

derives from the fact that the  $\nu=1 \rightarrow 2$  transition is of slightly lower energy than the  $\nu=0 \rightarrow 1$  transition. Therefore  $\Delta$  is a direct measurement of the anharmonicity of the oscillator. Were it

not for anharmonicity, the two spots would overlap and cancel, and there would be no spectroscopy at all.

### 2.1.5.2 Spectral Diffusion

One of the most informative pieces of data that comes from 2D IR, invisible with linear IR, is spectral diffusion. Recall from Section 2.1.1.1 that in the condensed phase, oscillators exist in a range of chemical environments. The upper left image in Figure 16 represents a prototypical absorption peak in the moment of excitation. The colored peaks are the Lorentzian response of the system, their width being termed the *homogeneous linewidth* (Figure 15).

The homogeneous linewidth is a consequence of the system response. A classical treatment of a harmonic oscillator yields a Lorentzian as an approximation to the solution of the system differential equation, but we also have a quantum explanation. Recall from Section 2.1.1.2 that we model the system response as an exponential decay in the time domain. The Fourier transform of this exponential into the frequency domain yields a Lorentzian curve

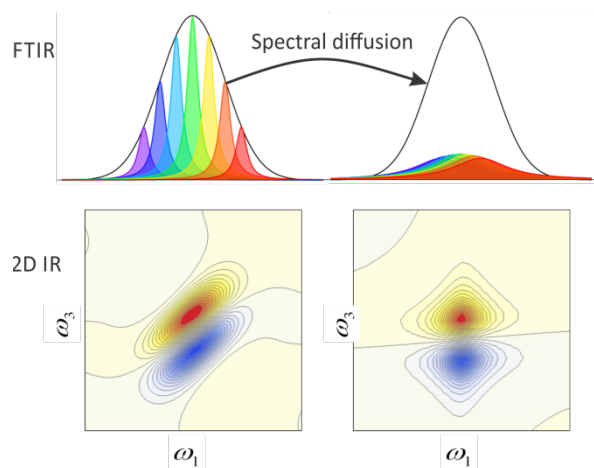


**Figure 16: Spectral diffusion**

(Section 1.01(a)(i)Appendix D). As the system dynamics become faster, the homogeneous linewidth broadens. As this is a system characteristic, no modification to the spectrometer can reduce it further.

An isolated Lorentzian response is almost never directly observable in the condensed phase because of variability in local environments, giving

a Gaussian distribution of Lorentzian lineshapes. The result is the convolution of Lorentzian and Gaussian shapes, most properly called a Voigt response, but generally treated as a Gaussian. The width of this distribution is called the *inhomogeneous linewidth*.

At the moment of excitation, the system is the state shown on the left side of Figure 16. Input frequency is highly correlated out output frequency because the oscillators have not yet had time to reorganize. As time progresses, the oscillators move into different environments, so that their new frequency does not match the one that excited it. The individual Lorentzian lineshapes broaden, drop in amplitude, and shift their peaks toward the center as local oscillator environments redistribute themselves. As the total energy is unchanged, only redistributed, the overall envelope remains the same as at the beginning, which is why linear IR is unable to resolve the process.

2D-IR, by correlating two sets of frequencies, is able quantify spectral diffusion measuring the time constant of the diffusion process through the shape of the spots, as they progress from highly elliptical to round or diamond-shaped. There are a number of methods to quantify the amount of spectral diffusion that has occurred, three of which are shown in Figure 17. The first (A) measures the ellipticity of the spots, the other two, (B and C) measure the centerline slope and nodal line slope, respectively. The measure of spectral diffusion is then calculated:

$$\Theta = \frac{a^2 - b^2}{a^2 + b^2} \quad m = \frac{a}{b} \quad 45$$

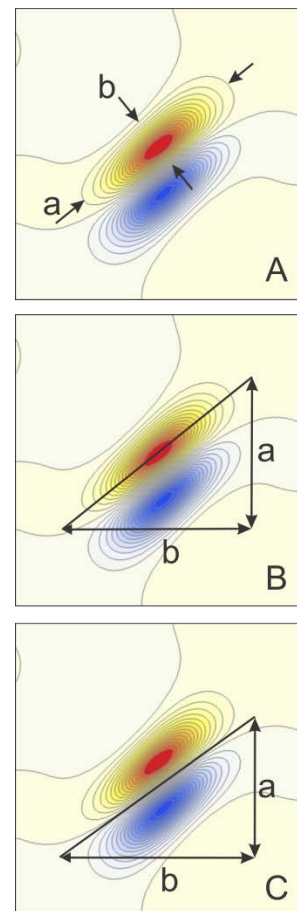


**Figure 17: Methods of measuring spectral diffusion**

These individual correlation values are plotted against population time and fitted to an exponential or bi-exponential function, the latter often being a better fit because more than one diffusion process is likely present. The time constants from the fitted curve reveal the time scales of the processes.

### 2.1.5.3 Cross Peaks

As in 2D NMR, 2D infrared spectroscopy may yield cross peaks, revealing a variety of information

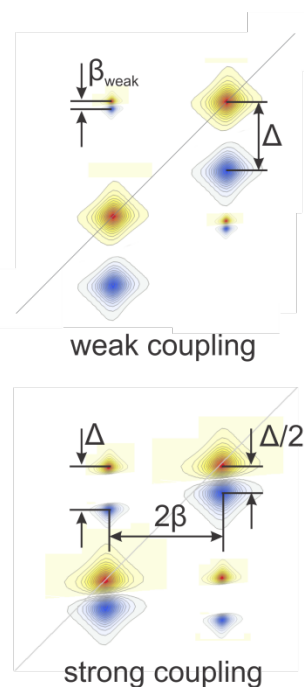


**Figure 18: Weak and strong coupling domains**

Static cross peaks appear even at short time scales when oscillators are coupled in vibrational excitons. Figure 18 shows an example system with two-oscillator coupling. Without going through the derivations (see Hamm and Zanni<sup>16</sup>)  $\Delta$  is the anharmonicity of the oscillator, and  $\beta$  is the coupling between them. As shown, the strength of the coupling manifests itself graphically and parameters can be measured directly from the spectrum.  $\beta_{weak}$  represents the magnitude of coupling in the weak limit and is approximated as

$$\beta_{weak} = -4\Delta \frac{\beta^2}{(\hbar\omega_2 - \hbar\omega_1)^2}. \quad 46$$

Dynamic cross peaks evolve over time, and in most cases appear after some dynamic process has taken place in the system. One of these is population transfer, which occurs when energy is transferred between different oscillators with similar energy levels.

Another process is chemical exchange where an oscillator starts out in one chemical environment, and after excitation moves to another chemical configuration. This is different

from spectral diffusion wherein an oscillator is moving around in a distribution of similar chemical environments, and instead represents a chemical process such as conformational reorganization or chemical binding.



### 3.0 MATERIALS AND METHODS

Samples were prepared of 200 mM butyramide and 250 mM EDTA-D<sub>8</sub> disodium along with 0, 2.5, and 5 M CaCl<sub>2</sub> and MgCl<sub>2</sub>. All three of the salts form hydrates, the chlorides being quite hygroscopic. CaCl<sub>2</sub> was dried at 260 °C and EDTA at 180 °C, and stored in a homemade desiccator. EDTA decomposes when heated in air to near its melting point. The acidic hydrogens of EDTA were replaced with deuterium by three cycles of dissolving anhydrous EDTA in D<sub>2</sub>O and evaporating, and the resulting EDTA deuterate used. MgCl<sub>2</sub> was purchased anhydrous and maintained tightly sealed.

The EDTA samples were adjust toward pH 12, as EDTA becomes less soluble with decreasing pH and because protonation of the nearby nitrogen atoms at lower pH disturbs the electron density within the carboxyl group, making it less representative of carboxyl groups in peptides. However, at pH 12, the 250 and 500 mM samples of CaCl<sub>2</sub> and MgCl<sub>2</sub> became cloudy, likely from the formation of insoluble hydroxides, and were adjusted back to pH 11 to obtain clear samples.

Linear spectra were taken with a Nicolet 6700 FTIR spectrometer using CaF windows and a 50 micron path length in a 1 mm-wide flow cell channel. Because H<sub>2</sub>O bending bands overlap the carbonyl and carboxyl asymmetric stretch bands we wish measure, all work was done in D<sub>2</sub>O.

Butyramide and the butyramide-calcium complex were studied with third-order 2D-IR spectroscopy. The instrument consists of a 100 fs, 5 kHz modelocked infrared laser at 800 nm provides the initial source of radiation in 1 mJ pulses. Approximately 200  $\mu\text{J}$  of its output is directed into an optical parametric amplifier (OPA) that uses two frequency mixing stages to generate a tunable output from nominally 3 to 8 microns ( $3300\text{-}1250\text{ cm}^{-1}$ )<sup>17</sup>. The resulting approximately 2  $\mu\text{J}$  pulse train is directed into the actual 2D spectrometer configured in a pump-probe geometry<sup>18</sup>. A 2x32 channel MCT detector acquires spectral data and supplies it to a computer for processing.

In our instrument, the first two (pump) pulses are collinear, which means  $k_1 - k_2 = 0$  for all pathways and that the emitted signal is in line with the third (probe) pulse. This arrangement greatly simplifies both construction and data processing because the rephasing and non-rephasing signals are added automatically at the detector.

The spectra were fit to a pair of 2D Gaussians for further processing.

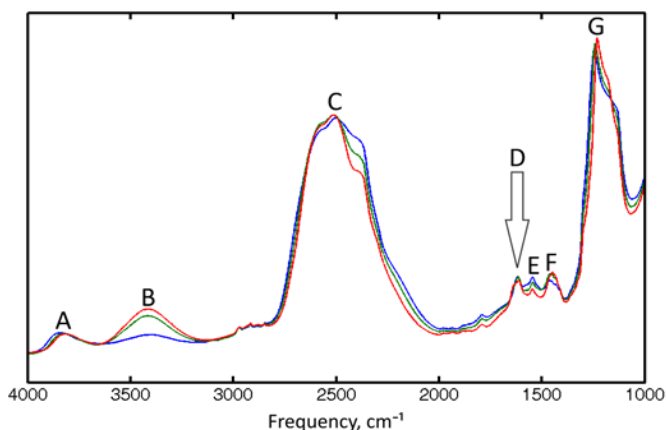
Bond lengths and normal mode frequencies in a simplified environment without solvent treatment were calculated with Q-Chem ([www.qchem.com](http://www.qchem.com)) using the b3lyp functional with a 6-31G\* basis set alone and bound to calcium and D<sub>2</sub>O.

## 4.0 RESULTS AND DISCUSSION

### 4.1 AMIDE

#### 4.1.1 General

The FTIR spectra of butyramide against an  $N_2$  background at the three concentrations of calcium ion are shown in Figure 19. The peaks are identified as follows: (A)  $D_2O$   $\nu_1+\nu_2+\nu_3$  combination band. (B) OH stretch. (C) OD stretch.



The shoulder on the red side is typical for this peak symmetric stretch, and the background.

change in amplitude is interpreted to result from various proportions of HOD as the amplitude changes correspond to those of peak B. (D) The amide I peak, which is the one of interest for this study. (E) May be an artifact of  $H_2O$  bending at  $1595\text{ cm}^{-1}$ , or of the combination band of  $D_2O$  bending and libration centered at  $1555\text{ cm}^{-1}$ . (F) may be HOD bend. (G) The  $D_2O$  bending peak at  $1178\text{ cm}^{-1}$ . The apparent peaks at  $1227$  and  $1238\text{ cm}^{-1}$  are interpreted as a saturation effect.

The corresponding plots for butyramide with calcium and magnesium are not significantly different at this scale.

A close-up of the amide I band, taken against a D<sub>2</sub>O with both Ca<sup>2+</sup> and Mg<sup>2+</sup> is shown in Figure 20, along with Gaussian fits to the two peaks. Both show an initial peak at 1620 cm<sup>-1</sup>. As salts are added, the peak red-shifts slightly to about 1616 cm<sup>-1</sup> and a blue-shifted shoulder

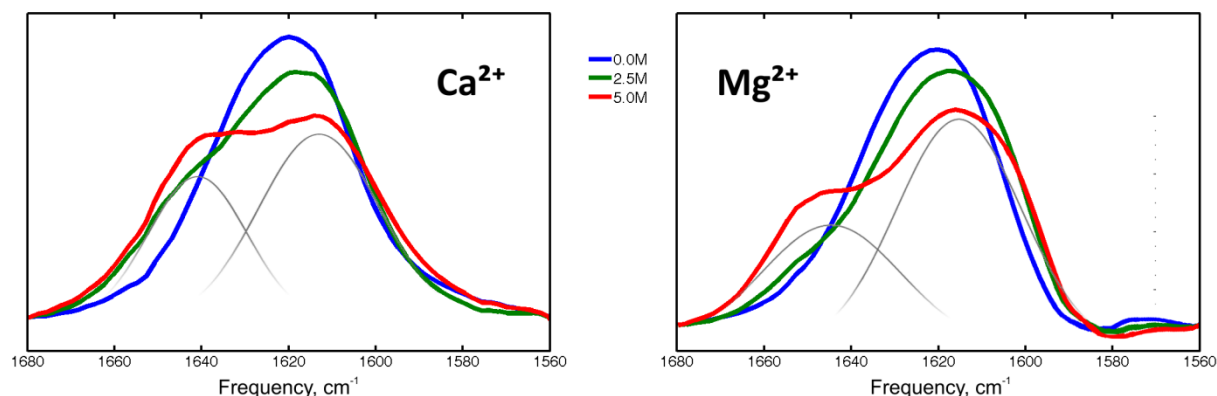


Figure 20: 200 mM butyramide in D<sub>2</sub>O with various concentrations of Ca<sup>2+</sup> and Mg<sup>2+</sup>

appears at 1645 cm<sup>-1</sup> with calcium and at 1649 cm<sup>-1</sup> with magnesium. The magnesium shoulder appears to not be as high, but this may be an artifact of the smaller overlap.

#### 4.1.2 Blue shift of butyramide amide I peak with salt concentration

The carbonyl peak of butyramide in D<sub>2</sub>O occurs at 1620 cm<sup>-1</sup>. With the addition of high concentrations of divalent cation, a second blue-shifted peak appears as shown above in Figure 20. A fit to Gaussians was performed using Mathematica, obtaining peaks at 1613 cm<sup>-1</sup> and 1649 cm<sup>-1</sup> for Ca<sup>2+</sup> and 1615 cm<sup>-1</sup> and 1649 cm<sup>-1</sup> for magnesium which are consistent with Cremer, et al.,'s fit at 1615 cm<sup>-1</sup> and 1645 cm<sup>-1</sup> for Ca<sup>2+</sup> and 1615 cm<sup>-1</sup> and 1649 cm<sup>-1</sup> for Mg<sup>2+</sup>. The relatively poor fit of Mg<sup>2+</sup> compared to Ca<sup>2+</sup> may be because of the baseline dip on those spectra,

interpreted to be an artifact of the background used. In both cases, as the secondary peak grows with concentration, the carbonyl-D<sub>2</sub>O peak decreases, yielding a clear indication of D<sub>2</sub>O displacement by the ion.

The amide I band occurs at 1718 cm<sup>-1</sup> in the vapor phase<sup>19</sup> and only appears at 1620 cm<sup>-1</sup> in D<sub>2</sub>O because of the red shift introduced by hydrogen bonding of water molecules through the shift of charge to the water  $\sigma^*$  orbitals. The apparent blue shift from the salts, therefore, is a relative shift due to the weaker red shift from the metal ions. Therefore, the apparent blue-shift with the cations is only relative, indicating a weaker binding than with water. If greater blue shift of Mg<sup>2+</sup> suggests that it binds more weakly than Ca<sup>2+</sup>. Both bind quite weakly as evidenced by the high concentrations required to get the secondary peak. Higher concentrations are not investigated because the ones used reflect the solubility limits of the salts.

### 4.1.3 Correlation Function

A series of 2D-IR spectra was taken of butyramide in D<sub>2</sub>O. The raw spectrum at a population time of 200 fs is shown in Figure 21. Pink areas are negative, representing decreased absorption from ground state bleach and stimulated emission, and the blue areas are positive, representing excited state absorption.

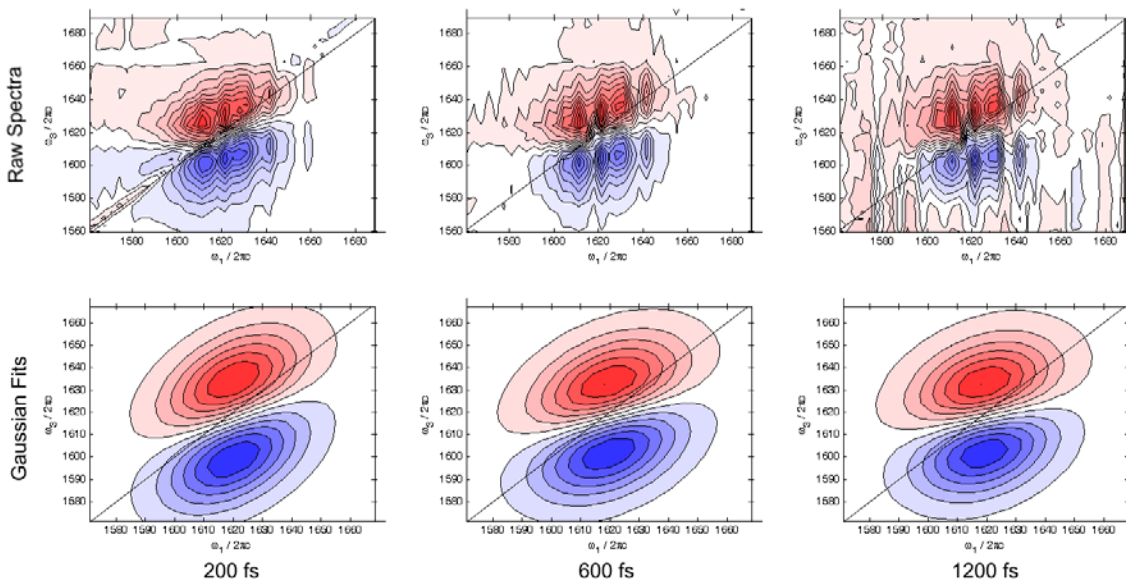


**Figure 21: Fitted 2D-IR spectra of butyramide in D2O at 200, 600, 1200 fs population time.**

The pink areas correspond roughly to peaks obtained from conventional linear spectroscopy, and in this case are not on the diagonal because of an error in the spectrometer calibration. The blue corresponds to the  $v=1$  to  $v=2$  transition. Measurements of this plot show a diagonal anharmonicity of about  $30 \text{ cm}^{-1}$ , a homogenous half-height width of about  $15 \text{ cm}^{-1}$ , and a single-standard-deviation inhomogeneous line width of about  $35 \text{ cm}^{-1}$ .

The gaps in both peaks are  $\text{H}_2\text{O}$  atmospheric absorption bands. Improving the quality of purge in the system is an ongoing struggle and improvements are still being made.

The ellipticity algorithm currently in use in our software failed with the butyramide data although it has worked well elsewhere. Software is not yet written to use

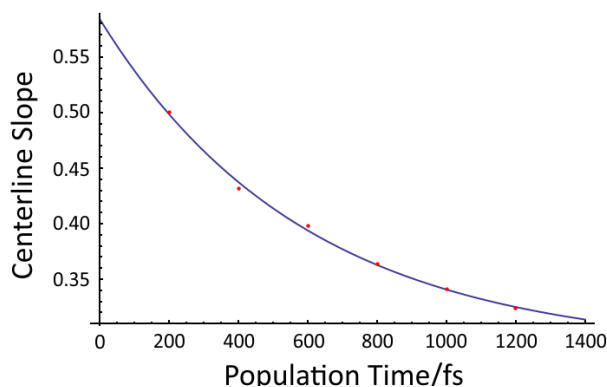


**Figure 22: Single-exponential correlation fit of butyramide/D<sub>2</sub>O spectral diffusion based on centerline slope.**

the centerline slope method. However, useable slope data could be extracted manually. An additional data point was available at 1400 fs, but the Gaussian fit was questionable (1600 was unusable) and yielded a spurious value. The data was fitted with Mathematica to a single exponential of the form

$$f = ae^{\frac{-t}{\tau}} + c. \quad 47$$

The plot of data points and the fitted curve is shown in Figure 22. The time constant  $\tau$  shows a timescale for the butyramide-water exchange dynamics of 600 fs.

#### 4.1.4 Red shift of butryamide-D<sub>2</sub>O amide I with salt concentration

My hypothesis to explain the red shift is based on exchange dynamics as diagrammed in Figure 23. These diagrams are intended to be representational and not an accurate portrayal of relative homogeneous and non-homogeneous lineshapes.

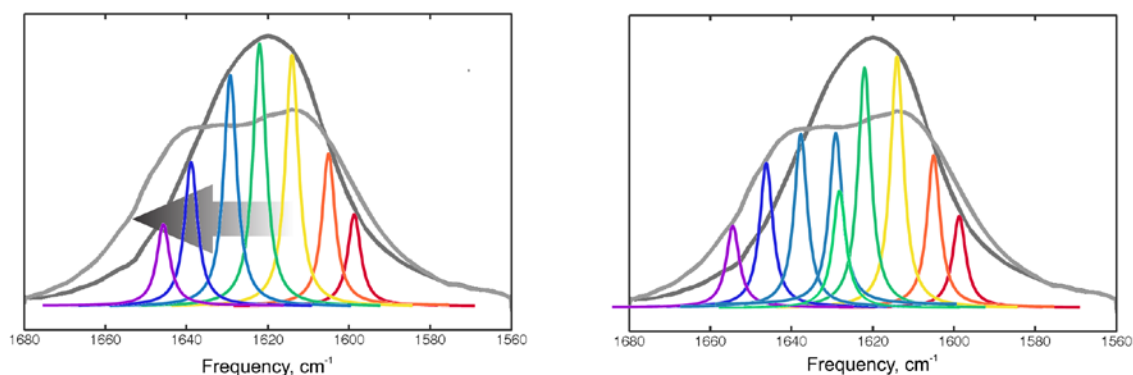


**Figure 23: Proposed spectral shift scenario in weak metal ion binding to butyramide**

The carbonyl absorption peak at  $1620 \text{ cm}^{-1}$  is the response of an ensemble of systems with varying degrees of interaction, those with stronger H-bonding with water corresponding to increased red shift to the right. Since the cations bind only weakly to the carbonyl, they can

compete more effectively with the more weakly bound water molecules leading to a greater depletion of their population. The amide-Ca band then appears (purple in the right-hand diagram) and the remaining resulting in a slightly red-shifted and reduced peak (red). This mechanism also explains the smaller peak amplitude changes with the weaker-binding magnesium.

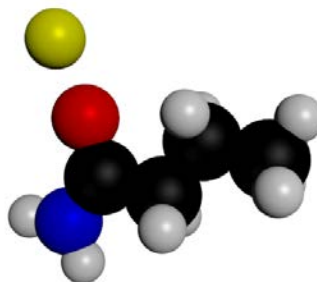
Note that at about  $1600\text{ cm}^{-1}$ , both ions show an increase in absorbance for the bound species. This is apparently not an artifact of the experiment since Cremer's data shows the same phenomenon. However, my data shows a larger difference in magnitude between the water-bound and ion-bound species for  $\text{Mg}^{2+}$ . This suggests an increase in the population of more strongly bound water molecules in the presence of the ions. It is not directly consistent with my hypothesis, but is consistent with Cremer's suggestion of hydration shell effects, as it is more pronounced with magnesium. It may be that two processes are working in conjunction and does not immediately invalidate my hypothesis.

My population dynamics hypothesis is only viable if the dynamics of cation-amide exchange are at least as fast as the  $\sim 2\text{ps}$  time scale<sup>20</sup> of water reorganization. Otherwise, unbound water populations would have time to re-equilibrate and restore the shape of the original peak. The  $600\text{ fs}$  time scale determined above for butyramide-water reorganization is certainly consistent with that interpretation. That the amide-ion binding is weak also suggests fast dynamics. Calculations by Mitchell<sup>21</sup> show that the amide-ion bond is weaker than either amide-water or water-water. 2DIR is an appropriate tool to test the hypothesis of chemical exchange by the timing of cross-peaks.



#### 4.1.5 Comparison with simulation results

Electronic structure calculations of a geometrically optimized model of butyramide (Figure 24) are compared with experimental results in Table 1. The vibrational frequencies were obtained directly from the output of Q-Chem, and the bond lengths obtained by importing the Q-Chem output into Avogadro and measuring the distances using Avogadro's built-in tool.  $\Delta\omega$  and  $\Delta E_{\text{SCF}}$  were calculated simply as the change in corresponding shifts from those of the  $\text{D}_2\text{O}$ -bound species.



Vibrational frequencies were calculated without anharmonicity in interest of computational economy and solvent effects are not accounted for. Therefore, the calculations represent more accurately the gas phase, and so frequencies are not expected to directly match those obtained experimentally. The shifts in frequency between bound and unbound states serve as the primary indicator. Interestingly, Cabannis, et al., obtained very similar results when performing these calculations with carboxylates using a PM3 parameter set with SPARTAN<sup>22</sup>. Nevertheless, the calculated shifts from water-bound to ion-bound species are comparable to the experimental values.

Simulations show a paradoxical lengthening of the amide carbonyl when bound to an ion, whereas the recorded blue shift relative to water would suggest a shortening of the bond.

**Table 1: Results of Q-Chem simulation of butyramide systems**

Species	Measured		Simulated (equivalent to gas phase)				
	$\omega/\text{cm}^{-1}$	$\Delta\omega/\text{cm}^{-1}$	$\omega/\text{cm}^{-1}$	$\Delta\omega/\text{cm}^{-1}$	$E_{\text{SCF}}/E_h$	$\Delta E_{\text{SCF}}/E_h$	C=O/pm
D <sub>2</sub> O	1620		1832.08	-	-364.26	-	123.0
Ca <sup>2+</sup>	1645	25	1852.77	20.69	-964.90	-600.64	128.9
Mg <sup>2+</sup>	1649	29	1852.23	20.15	-487.30	-123.04	128.9

## 4.2 CARBOXYLATE

### 4.2.1 General

EDTA has long been known to be a strong calcium chelating agent, and its ion binding characteristics have been extensively studied by Sawyer<sup>23,24</sup>, Lanigan<sup>25</sup>, Kovács<sup>26</sup>, and others.

Linear IR spectra are available for both calcium- and magnesium-bound species.

The FTIR spectra of the EDTA salts is similar to those for butyramide (Figure 25). Peak F is not simply the same D<sub>2</sub>O combination peak as identified in the butyramide spectrum, as it is higher in magnitude and

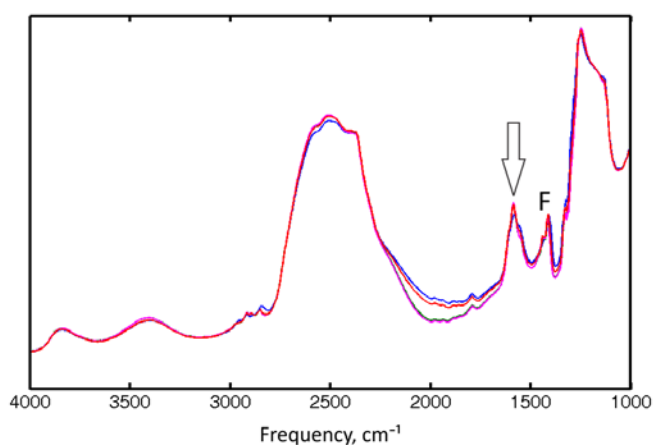


**Figure 25: FTIR spectra of EDTA/Mg<sup>2+</sup> at various concentrations of Mg<sup>2+</sup>**

resolves into two peaks, the larger somewhat red-shifted. That contributor is identified as the

carboxylate symmetric stretch. The similarly positioned carboxylate asymmetric stretch band is more prominent than the amide I band in butyramide, not surprising since EDTA has four chromophores per molecule.

Closeups of the EDTA asymmetric stretch in a fully deprotonated state with calcium and magnesium at pH 12 is shown in Figure 26. EDTA shows carboxylate asymmetric stretch at

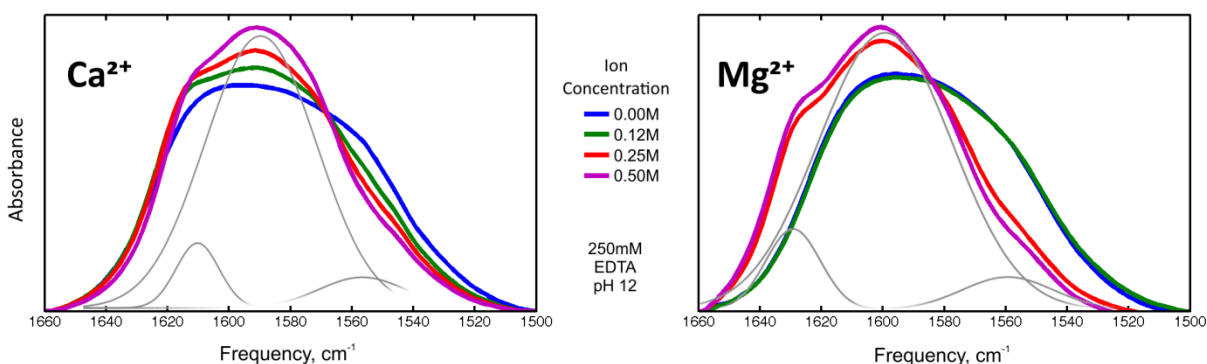


**Figure 26: FTIR spectra of 250mM EDTA-D 4 in D<sub>2</sub>O with various concentrations of Ca<sup>2+</sup> and Mg<sup>2+</sup> with D<sub>2</sub>O background**

1585 cm<sup>-1</sup>, shifting to 1589 cm<sup>-1</sup> for Ca<sup>2+</sup> and 1587 cm<sup>-1</sup> for Mg<sup>2+</sup> with the addition of up to 2 molar equivalents of metal ion.

A broad peak occurs at 1550 cm<sup>-1</sup> and does not shift with the addition of metal. This frequency corresponds to the same D<sub>2</sub>O bending and libration band as mentioned above. Although it does not shift in frequency, it drops rapidly in magnitude. A third peak appears at 1610 cm<sup>-1</sup> for Ca<sup>2+</sup> and 1600 cm<sup>-1</sup> for Mg<sup>2+</sup>.

## 4.2.2 Blue shift of EDTA carboxylate asymmetric stretch peak with salt concentration

EDTA is a more complicated system than butyramide not only because of eight possible binding sites but because it exists in six protonation states dependent on  $\text{pH}^{27}$  as shown in Figure 27.

Sawyer showed that the amine nitrogen atoms remain protonated at higher pH levels and dissociate last. Although all four carboxylates are deprotonated at physiological pH, inductive coupling from the positively charged amines

shifts charge from the partially occupied  $\pi^*$  orbitals of the adjacent carboxylates. This would result in a lower charge density than is present in carboxylates at physiological pH and give results inconsistent with *in vivo* binding behavior because of the difference in frequencies.

Magnesium's smaller blue shift suggests that it binds with EDTA more weakly than calcium. This is in agreement with literature, given the binding constants for  $\text{Ca}^{2+}$  and  $\text{Mg}^{2+}$  being  $5.0 \times 10^{10}$  and  $4.9 \times 10^8$ , respectively.

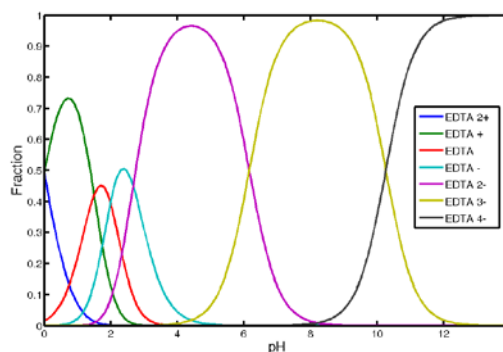


Figure 27: Protonation states of EDTA

## 4.2.3 Simulation Results

### 4.2.3.1 General Considerations

EDTA, being a tetracarboxylate system is expected to support vibrational excitons. As the electronic structure calculations of Q-Chem return

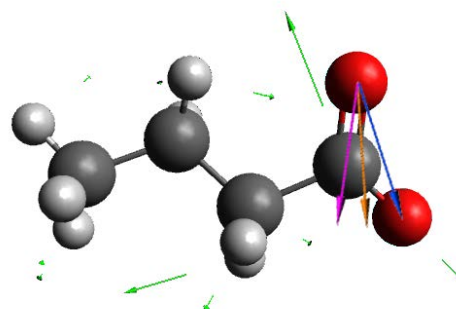
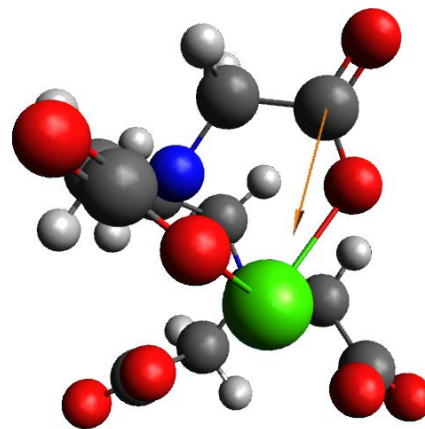


Figure 28: Local mode motions derived from a butyrate model

normal mode vibrations and normal modes are computationally intractable in excitonic systems, it is prudent to consider a local mode perspective.

To this end, electronic structure calculations of butyrate were analyzed with Mathematica to yield approximate data for local mode behavior in EDTA (Figure 28). The carboxylate asymmetric stretch at 1744.76 cm<sup>-1</sup> has a dipole moment of 784 Debye in a direction (orange) 14.08° off the axis connecting the two oxygen atoms (blue). This is very close to the angle halfway to the axis of one C=O bond, and so the bisected vector was taken as a close approximation to the actual



**Figure 29: Determination of local-mode dipole in EDTA complex**

dipole. Inspection of the molecular geometry of the EDTA-ion complex shows axis from the carbon to the metal ion is a good approximation for the direction of the local-mode transition dipole moment. Its magnitude remains that calculated for butyrate.

#### 4.2.3.2 Comparison of Experimental and Computational Results

The experimental data for EDTA is compared with electronic structure calculations in Table 2. The calculated values shown for carboxyl asymmetric stretch are those for the central frequency as Q-Chem returned four corresponding to carboxylate vibrational modes. Furthermore, as the EDTA/water simulation is still waiting in the queue as of the time of this writing, butyrate/water was used to establish the vibrational frequency of the unbound carboxylate. As the more planar structure of unbound EDTA places the dipoles either at two to three times the distance as in the bound species or at nearly right angles, anticipating

approximately an order of magnitude lower coupling between them, this approximation was deemed tenable.

**Table 2: Measured vs simulated results for EDTA binding**

Species	Measured		Simulated (equivalent to gas phase)		
	$\omega/\text{cm}^{-1}$	$\Delta\omega/\text{cm}^{-1}$	$\omega/\text{cm}^{-1}$	$\Delta\omega/\text{cm}^{-1}$	C=O/pm
D <sub>2</sub> O	1585		1703.94		
Ca <sup>2+</sup>	1589	4	1744.50	40.56	125.7
			1750.91	46.97	
			1752.48	48.54	
			1775.84	71.90	
Mg <sup>2+</sup>	1587	2	1753.27	49.33	122.9
			1762.79	58.85	
			1764.75	60.81	
			1791.39	87.45	

At once, we observe three interesting features. First, the calculated frequency shifts between the bound and unbound states are at least an order of magnitude greater than the experimental values. This may be, in part, a result of butyrate being a poor approximation to unbound EDTA. Second, the calculated shift for the Mg<sup>2+</sup> species is greater than for the Ca<sup>2+</sup> species, whereas the reverse is true experimentally. This discrepancy is not understood. Third, the splitting demonstrated by the Mg<sup>2+</sup> species is somewhat greater than for the Ca<sup>2+</sup> species, suggesting tighter coupling.

The four vibrational modes are shown graphically in Figure 30. Because they look

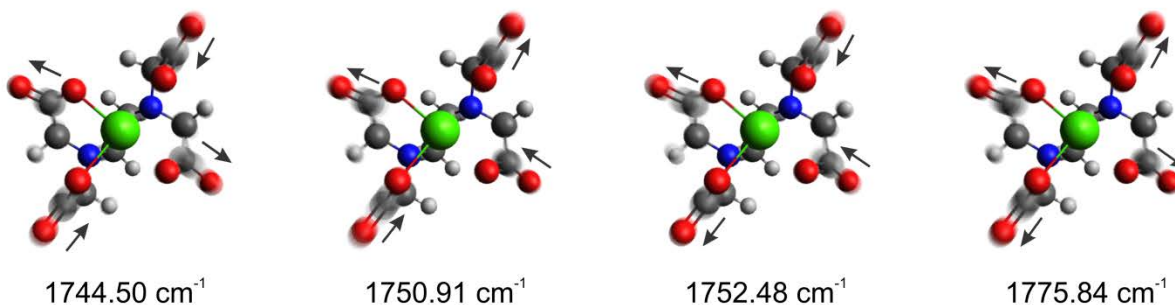


**Figure 30: Vibrational modes of EDTA corresponding to the carboxylate-Ca asymmetric stretch frequencies as calculated by Q-Chem.**

identical in a static representation, phase arrows have been added. The vibrational frequencies for both ions are listed in

Table 3 and shown as stick plots in Figure 32. They ranged from 1764.01 to 1841.09  $\text{cm}^{-1}$  for EDTA bound to  $\text{Ca}^{2+}$  and 1779.90 to 1842.17  $\text{cm}^{-1}$  bound to  $\text{Mg}^{2+}$ .

**Table 3: Calculated spectroscopic bands corresponding to carboxylate asymmetric stretch.**

$\text{Ca}^{2+}$		$\text{Mg}^{2+}$	
$\omega / \text{cm}^{-1}$	Amplitude (km/mole)	$\omega / \text{cm}^{-1}$	Amplitude (km/mole)
1744.50	177.974	1753.27	177.974
1750.91	1065.271	1762.79	1209.355
1752.48	1569.919	1764.75	1427.892
1775.84	106.616	1791.39	32.224

The stick plots show similar vibrational patterns for both species. They show a pair of closely spaced frequencies containing most of the energy, a weaker emission on the red-shifted side, and an even weaker one farther away on the blue-shifted side.

The relative strength of the peaks can be explained using a symmetry argument. Although a  $C_2$  rotational symmetry was necessary to determine the identity of coupling constants, a  $C_4$  rotational symmetry better describes the vibrational modes (Figure 31).

Recording the change in sign of the vibrational modes with each  $90^\circ$  rotation we can identify

the number of nodes for each case. We know from fundamental group theory that of these cases, only those with one node are consistent with infrared activity. The “forbidden” cases of two and zero nodes then represent the small signals at the high and low ends of Figure 32. They are not quite zero because the symmetry is not exact.

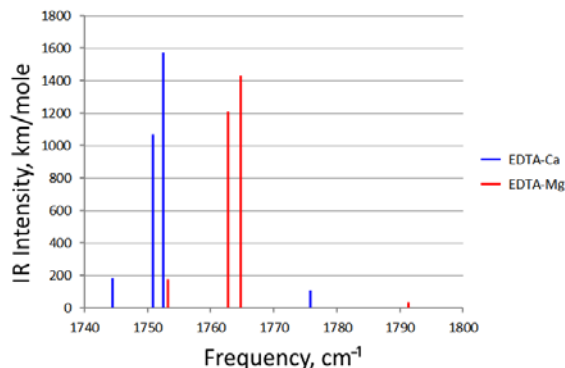


Figure 32: Stick plot of EDTA carboxylate antisymmetric stretch frequencies

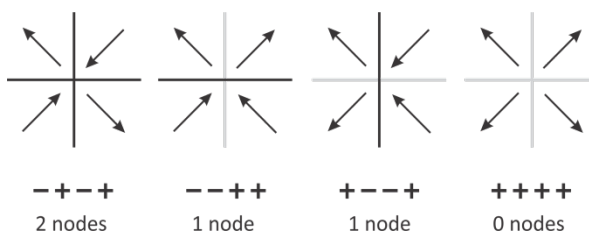


Figure 31: Rotational symmetry of EDTA vibrational modes

#### 4.2.4 Initial investigation into EDTA vibrational excitons

EDTA has four equivalent carboxylates, so the molecule, barring distortions, exhibits a  $C_2$  symmetry as shown in Figure 33. Therefore, the transition dipole coupling between adjacent

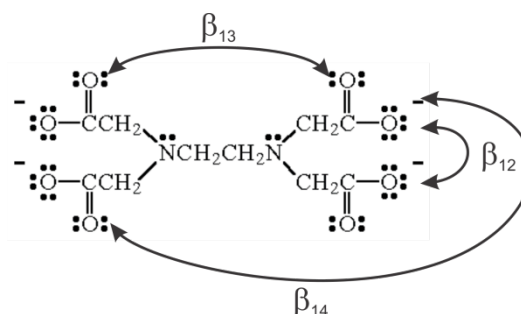


Figure 33: Schematic of EDTA



oscillators in either direction are not equivalent. This suggests that the single-quantum Hamiltonian, using the coupling coefficients  $\beta_{ij}$  as indicated in the figure, is best represented as

$$H = \begin{pmatrix} \varepsilon & \beta_{12} & \beta_{13} & \beta_{14} \\ \beta_{12} & \varepsilon & \beta_{14} & \beta_{13} \\ \beta_{13} & \beta_{14} & \varepsilon & \beta_{12} \\ \beta_{14} & \beta_{13} & \beta_{12} & \varepsilon \end{pmatrix}, \quad 48$$

where  $\varepsilon$  corresponds to the frequency of the uncoupled vibrational modes, and  $\beta_{12}$ ,  $\beta_{13}$ , and  $\beta_{14}$  are the coupling constants with neighbors in order of distance.

Hamm and Zanni give the coupling between two dipoles as

$$\beta_{ij} = \frac{1}{4\pi\varepsilon_0} \left[ \frac{\vec{\mu}_i \cdot \vec{\mu}_j}{r_{ij}^3} - 3 \frac{(\vec{r}_{ij} \cdot \vec{\mu}_i)(\vec{r}_{ij} \cdot \vec{\mu}_j)}{r_{ij}^5} \right], \quad 49$$

where  $\vec{\mu}_i$  and  $\vec{r}_i$  are the transition dipoles and their positions, respectively.

However, as important as this model is for the physical picture of oscillator coupling, it can be often be more accurately calculated by fitting the Hamiltonian (Equation

$$H = \begin{pmatrix} \varepsilon & \beta_{12} & \beta_{13} & \beta_{14} \\ \beta_{12} & \varepsilon & \beta_{14} & \beta_{13} \\ \beta_{13} & \beta_{14} & \varepsilon & \beta_{12} \\ \beta_{14} & \beta_{13} & \beta_{12} & \varepsilon \end{pmatrix}, \quad 48 \text{ in this case) to the known energy eigenvalues. This was done$$

with MATLAB script, and the resulting parameters verified with a Mathematica script (Appendix E). The results (Table 4) show the greatest difference between the two systems being between the closest oscillators.

**Table 4: Computed coupling values for EDTA systems.**

Coupling	Ca <sup>2+</sup>	Mg <sup>2+</sup>
	$\omega$ /cm-1	$\omega$ /cm-1
$\epsilon$	1755.7	1768.1
$\beta_{12}$	-7.2	-10.0
$\beta_{13}$	-4.4	-4.3
$\beta_{14}$	8.4	8.4

The discrepancy between coupling constants obtained through geometrical methods versus solution of the Hamiltonian suggest inadequacies in the physical model used for the geometrical method. Possibilities for error include poor assumptions on the local-mode transition dipole axis and position and the butyramide model not yielding an appropriate estimate of the magnitude of the transition dipole moment.

These binding constants can be used to perfect the geometrical model described in

$$\text{Equation } \beta_{ij} = \frac{1}{4\pi\epsilon_0} \left[ \frac{\vec{\mu}_i \cdot \vec{\mu}_j}{r_{ij}^3} - 3 \frac{(\vec{r}_{ij} \cdot \vec{\mu}_i)(\vec{r}_{ij} \cdot \vec{\mu}_j)}{r_{ij}^5} \right], \quad 49.$$

In addition, accurate treatment in regard to 2D infrared spectroscopy requires consideration of the two-quantum Hamiltonian, which is not yet developed for EDTA.

## 5.0 CONCLUSION

This work has confirmed much of the literature data regarding amide and EDTA binding to alkaline earth metals. Unfortunately, difficulty with the 2D instrument to date has interfered with the collection of reliable data to begin addressing the questions posed in the introduction. Nevertheless, some observations can be made.

The absence of a dramatic difference between the behaviors of  $\text{Ca}^{2+}$  and  $\text{Mg}^{2+}$  suggests that they would bind similarly in EF-hand. Since we know that EF-hand is often highly specific for calcium<sup>28</sup>, it is evident that this selectivity arises from cooperativity of binding units in EF-hand and not from characteristics of any one ligand.

The computational studies of EDTA show clear energy-splitting effects due to vibrational excitons despite the fact that the transition dipoles are not aligned conveniently. Therefore, it is reasonable to hypothesize that excitons do play a role in the dynamics of EF-hand, as their dipoles are aligned comparably

## APPENDIX A

### DERIVATION OF THE LIOUVILLE-VON NEUMANN EQUATION FOR A STATISTICAL ENSEMBLE

The standard form of the Schrödinger equation,

$$-\frac{i}{\hbar} \frac{\partial}{\partial t} |\psi\rangle = \hat{H} |\psi\rangle \quad 50$$

implies its complex conjugate,

$$\frac{i}{\hbar} \frac{\partial}{\partial t} \langle\psi| = \langle\psi| \hat{H}^* \quad 51i$$

A density matrix of an ensemble of states is

$$\rho = \sum_i p_i |\psi_i\rangle \langle\psi_i| \quad 52$$

where  $p_i$  is the population fraction of the  $i$ th contributing state. Using the chain rule, we can expand the time-dependent Schrödinger equation for the ensemble.

$$\begin{aligned} -\frac{i}{\hbar} \rho &= \sum_i p_i |\psi_i\rangle \langle\psi_i| \\ &= \sum_i p_i |\psi_i\rangle \frac{\partial}{\partial t} \langle\psi_i| + \sum_i p_i \left( \frac{\partial}{\partial t} \right) |\psi_i\rangle + \sum_i \left( \frac{\partial}{\partial t} p_i \right) |\psi_i\rangle \langle\psi_i| \end{aligned} \quad 53$$

Substituting first (i) and (ii), then (iii), we arrive at

$$\begin{aligned}
-\frac{i}{\hbar} \frac{\partial}{\partial t} \rho &= -\sum_i p_i |\psi_i\rangle \langle \psi_i| \hat{H}^* + \sum_i p_i \hat{H} |\psi_i\rangle \langle \psi_i| + \sum_i \left( \frac{\partial}{\partial t} p_i \right) |\psi_i\rangle \langle \psi_i| \\
&= -\rho \hat{H}^* + \hat{H} \rho + \sum_i \left( \frac{\partial}{\partial t} p_i \right) |\psi_i\rangle \langle \psi_i|
\end{aligned} \tag{54}$$

Recognizing that the Hamiltonian, like all quantum mechanical operators, must be Hermitian, and therefore that  $\hat{H}^* = \hat{H}$ , we can write it in the more compact commutator notation:

$$-\frac{i}{\hbar} \frac{\partial}{\partial t} \rho = [\hat{H}, \rho] + \sum_i \left( \frac{\partial}{\partial t} p_i \right) |\psi_i\rangle \langle \psi_i| \tag{55}$$

Excluding the summation term at the right, this is the canonical form of the Liouville-von Neumann equation. The rightmost term is a thermodynamic term that expresses the change in populations of the various individual states over time. We know from statistical thermodynamics that the highest entropy occurs when the members of any energy level are evenly distributed over the available states. Therefore, the configuration will drift in that direction. This is the mathematical origin of the dephasing phenomenon. Because there are an infinite number of possible states (or practically infinite as far as computation is concerned) we have no method to deal with this term, we instead resort to the phenomenological models mentioned in this paper.

## APPENDIX B

### THIRD-ORDER RESPONSE FUNCTIONS

$$R_1(t_1, t_2, t_3) \propto i\mu_{01}^4 e^{+i\omega_0 t_1} e^{-t_1/T_2} e^{-t_2/T_1} e^{-i\omega_0 t_3} e^{-t_3/T_2} \quad 56$$

$$R_2(t_1, t_2, t_3) \propto i\mu_{01}^4 e^{+i\omega_0 t_1} e^{-t_1/T_2} e^{-t_2/T_1} e^{-i\omega_0 t_3} e^{-t_3/T_2} \quad 57$$

$$R_3(t_1, t_2, t_3) \propto -i\mu_{01}^2 \mu_{12}^2 e^{+i\omega_0 t_1} e^{-t_1/T_2^{(01)}} e^{-t_2/T_1} e^{-i\omega_0 t_3} e^{-t_3/T_2^{(12)}} \quad 58$$

$$R_4(t_1, t_2, t_3) \propto i\mu_{01}^4 e^{-i\omega_0 t_1} e^{-t_1/T_2} e^{-t_2/T_1} e^{-i\omega_0 t_3} e^{-t_3/T_2} \quad 59$$

$$R_5(t_1, t_2, t_3) \propto i\mu_{01}^4 e^{-i\omega_0 t_1} e^{-t_1/T_2} e^{-t_2/T_1} e^{-i\omega_0 t_3} e^{-t_3/T_2} \quad 60$$

$$R_6(t_1, t_2, t_3) \propto -i\mu_{01}^2 \mu_{12}^2 e^{-i\omega_0 t_1} e^{-t_1/T_2^{(01)}} e^{-t_2/T_1} e^{-i\omega_0 t_3} e^{-t_3/T_2^{(12)}} \quad 61$$

## APPENDIX C

### FEYNMAN DIAGRAM RULES

1. Time runs from the bottom to the top.
2. The time evolution must end at a population state. In linear spectroscopy, this will be the ground state  $|0\rangle\langle 0|$ , but in nonlinear spectroscopy may be another population state. Typically, evolutions begin at the ground state, but this is not a requirement, and that initial state is sometimes omitted.
3. Interactions with the field are indicated by arrows. The direction of the arrow indicates the time propagation of the wave and the side on which it appears indicates action on the bra or ket. More explicitly, an arrow pointing to the right indicates a wave of the form  $e^{-i\omega t + i\vec{k}\vec{r} + \phi}$  and an arrow pointing to the left indicates a wave of the form  $e^{+i\omega t - i\vec{k}\vec{r} + \phi}$ .
4. The emitted field is shown as a dashed arrow.
5. By convention, complex conjugates are not drawn, as they contain no additional information. By the same convention, the one is drawn that shows the emitted field at the top left.

6. Each diagram has a sign  $(-1)^n$ , where  $n$  is the number of arrows on the right. This sign derives from the commutators expansion discussed in the text. The emitted field arrow is never counted, as it does not derive from the commutators.
7. An arrow pointing in toward the system represents an increase in the eigenstate of the bra or ket, and an arrow point out represents a decrease. This is consistent with the exclusions of the rotating wave approximation.



## APPENDIX D

### THE FOURIER TRANSFORM

#### D.1 GENERAL INFORMATION

Fourier transforms are widely used in communications theory and engineering to transform signals back and forth between time and frequency domains. In more general terms, it converts a function from a set of units to the corresponding function in reciprocal units. In spectroscopy, Fourier transforms of the exponential and Gaussian functions are particularly interesting.

#### D.2 RELEVANT EXAMPLES

##### D.2.1 Exponential

The Fourier transform of an incomplete exponential is given by

$$\mathcal{F}_t \left[ e^{-2\pi\omega_0 t} \right] = \frac{1}{\pi} \frac{\omega_0}{\omega^2 - \omega_0^2} \quad \mathbf{62}$$

The parameter  $\omega_0$  specifies the decay rate of the exponential, the higher  $\omega_0$ , the faster the decay. After the transform,  $\omega_0$  appears in both the numerator and the denominator, but is squared in the latter. Therefore, an increasing  $\omega_0$



**Figure 34: Right-handed exponential function**

causes the denominator to grow faster, leading to a narrower pulse.

Note that this transform is not for a complete exponential, because that one doesn't behave well. Specifically, this is for right-handed exponential (**Figure 34: Right-handed exponential function**), which is exactly the exponential envelope that interests us in 2D IR spectroscopy.

Interestingly, it is possible to take the Fourier transform of the entire exponential:

$$\mathcal{F}_t \left[ e^{-2\pi\omega_0 t} \right] = \sqrt{2\pi} \delta(2i\omega_0 + \omega) \quad 63$$

This case yields a Dirac delta function, which is intuitive, as the Dirac delta is the limiting case for an increasingly narrow pulse.

## D.2.2 Gaussian

The Fourier transform of a Gaussian is given by

$$\mathcal{F}_t \left[ \frac{1}{\sigma\sqrt{2\pi}} e^{-\frac{t^2}{2\sigma^2}} \right] = \frac{1}{\sqrt{2\pi}} e^{-\frac{\omega^2\sigma^2}{2}}. \quad 64$$

Note that the Fourier transform is still a Gaussian, but that the standard deviation  $\sigma$  translates from the denominator to the numerator. Therefore a wide Gaussian transforms to a narrow one and vice-versa.

## APPENDIX E

### CODE RELATED TO EDTA COUPLING PARAMETERS

#### E.1.1 MATLAB code for calculating coupling constants<sup>1</sup>

```
%% fit qchem
expt = [1753.27 1762.79 1764.75 1791.39]';
p0 = [1750 -12 -5 10];
%options = optimset('fminsearch'); %get default options
%options = optimset(options,'Display','iter','TolFun',1e-12,'TolX',1e-8)

pfit = fminsearch(@(p) EDTA_eigenval_err(p,expt),p0)

EDTA_eigenval(pfit)
```

---

<sup>1</sup> Courtesy of Sean Garrett-Roe

```

function [out,vec] = EDTA_eigenval(p)

alpha = p(1);
beta_12 = p(2);
beta_13 = p(3);
beta_14 = p(4);

H = [alpha beta_12 beta_13 beta_14;
     beta_12 alpha beta_14 beta_13;
     beta_13 beta_14 alpha beta_12;
     beta_14 beta_13 beta_12 alpha];

if nargin == 1
out = eig(H);
out = sort(out);
else if nargin == 2
    [vec,out]=eig(H);
    out = diag(out);
    end
end

function err = EDTA_eigenval_err(p,expt)
%function err = EDTA_eigenval_err(p1,p2,p3,p4,expt)
%calc = EDTA_eigenval([p1 p2 p3 p4]);
calc = EDTA_eigenval(p);
err = sum((expt-calc).^2);

```

## E.1.2 Mathematica code for validating coupling constants

```
 $\beta_{12} = -7.2;$   
 $\beta_{13} = -4.4;$   
 $\beta_{14} = 8.4;$   
 $\epsilon = 1755.70;$   
 $h = \{ \{ \epsilon, \beta_{12}, \beta_{13}, \beta_{14} \}, \{ \beta_{12}, \epsilon, \beta_{14}, \beta_{13} \}, \{ \beta_{13}, \beta_{14}, \epsilon, \beta_{12} \},$   
   $\{ \beta_{14}, \beta_{13}, \beta_{12}, \epsilon \} \};$   
 $\{ \text{vals}, \text{vecs} \} = \text{Eigensystem}[h];$   
 $\text{vecs.h.Transpose}[\text{vecs}]$   
 $\{ \{ 1775.7, 1.13687 \times 10^{-13}, 3.97904 \times 10^{-13}, 3.97904 \times 10^{-13} \},$   
   $\{ 1.13687 \times 10^{-13}, 1752.5, -2.84217 \times 10^{-13}, -3.97904 \times 10^{-13} \},$   
   $\{ 5.11591 \times 10^{-13}, -2.84217 \times 10^{-13}, 1750.1, 0. \},$   
   $\{ 3.41061 \times 10^{-13}, -5.11591 \times 10^{-13}, 1.13687 \times 10^{-13}, 1744.5 \} \}$   
  
 $\beta_{12} = -10.0;$   
 $\beta_{13} = -4.3;$   
 $\beta_{14} = 8.4;$   
 $\epsilon = 1768.1;$   
 $h = \{ \{ \epsilon, \beta_{12}, \beta_{13}, \beta_{14} \}, \{ \beta_{12}, \epsilon, \beta_{14}, \beta_{13} \}, \{ \beta_{13}, \beta_{14}, \epsilon, \beta_{12} \},$   
   $\{ \beta_{14}, \beta_{13}, \beta_{12}, \epsilon \} \};$   
 $\{ \text{vals}, \text{vecs} \} = \text{Eigensystem}[h];$   
 $\text{vecs.h.Transpose}[\text{vecs}]$   
 $\{ \{ 1790.8, -5.68434 \times 10^{-14}, 0., -1.13687 \times 10^{-13} \},$   
   $\{ -1.13687 \times 10^{-13}, 1765.4, -3.41061 \times 10^{-13}, 2.84217 \times 10^{-13} \},$   
   $\{ -1.13687 \times 10^{-13}, -3.97904 \times 10^{-13}, 1762.2, 1.13687 \times 10^{-13} \},$   
   $\{ 0., 1.13687 \times 10^{-13}, 1.7053 \times 10^{-13}, 1754. \} \}$ 
```

## BIBLIOGRAPHY

1. Berridge, M. J.; Lipp, P.; Bootman, M. D. *Mol. Cell Biol.* 2000, 1..
2. Kahl, C. R. *Endocr. Rev.* 2003, 24, 719–736.
3. McPhalen, C. A.; Strynadka, N. C. J.; James, M. N. W. *Advan. Protein Chem.* 1991, 42, 77-144.
4. Gentry, H. R.; Singer, A. U.; Betts, L.; Yang, C.; Ferrara, J. D.; Sondek, J.; Parise, L. V J. *Biol. Chem.* 2005, 280, 8407–15.
5. Cates, M. S.; Berry, M. B.; Ho, E. L., Li, Q.; Potter, J. D.; Phillips, G. N. *Struct. Fold. Des.* 1999, 7, 1269–1278.
6. Okur, H. I.; Kherb, J.; Cremer, P. S. J. *Am. Chem. Soc.* 2013.
7. Laage, D.; Stirnemann, G.; Hynes, J. T. J. *Photochem. Photobiol. A Chem.* 2012, 234, 75–82.
8. Reed, A. E.; Curtiss, L. a.; Weinhold, F. *Chem. Rev.* 1988, 88, 899–926.
9. Loomis, L. D.; Raymond, K. N. *Inorg. Chem.* 1991, 30, 906–911.
10. Bruni, F.; Imberti, S.; Mancinelli, R.; Ricci, M. a J. *Chem. Phys.* 2012, 136, 064520.
11. Persson I.; Sandström M.; Yokoyama H.; Chaudhry M. Z. *Naturforsch., Teil A* 1995, 50, 21–37.
12. Bhattacharya, S.; Bunick, C. G.; Chazin, W. J. *Biochim. Biophys. Acta* 2004, 1742, 69–79.

13. Grabarek, Z. *Biochim. Biophys. Acta.* 2011, 1813, 913–921.
  14. Laage, D.; Stirnemann, G.; Hynes, J. T. *J. Photochem. Photobiol. A Chem.* 2012, 234, 75–82.
  15. Heinze, G; Hubrich, C; Halfmann, T. *Phys. Rev. Lett.*, 2013, 111.
  16. Hamm, P.; Zanni, M. *Concepts and Methods of 2D Infrared Spectroscopy*; Cambridge: Cambridge, 2011
  17. Hamm, P.; Lauterwasser, C.; Zinth, W. *Opt. Lett.* 1993, 18, 1943–1945.
  18. Helbing, J.; Hamm, P. *J. Opt. Soc. Am. B* 2011, 28, 171.
  19. Balasubramanian, D.; Shaikh, R. *Biopolymers* 1973, 12, 1639–1650.
  20. Garrett-Roe, S.; Hamm, P. *Phys. Chem. Chem. Phys.* 2010, 12, 11263–6.
  21. Mitchell, J. B. O.; Price, S. L. *Chem. Phys. Lett.* 1991, 180, 517–523.
  22. Cabaniss, S. E.; McVey, I. F. *Spectrochim. Acta Part A Mol. Biomol. Spectrosc.* 1995, 51, 2385–2395.
  23. Sawyer, T. J. *Am. Chem. Soc.* 1958, 80, 1597–1600.
  24. Sawyer, D. T. *Ann. N. Y. Acad. Sci.* 1960, 88, 307–321.
  25. Lanigan, K. C.; Pidosny, K. *Vib. Spectrosc.* 2007, 45, 2–9.
  26. Kovács, A.; Nemcsok, D. S.; Kocsis, T. J. *Mol. Struct. THEOCHEM* 2010, 950, 93–97.
- Nakamoto, K.; Morimoto, Y.; Martell, A. E. *J. Am. Chem. Soc.* 1963, 85, 309–313.